



Encoding of Qubit States in Resonators With Cat Codes

A Proof of Concept for Numerically Optimizing Encoding
Pulses Using Krotov's Method

Master's thesis in Nanotechnology

JOHAN WINTHER

MASTER'S THESIS IN NANOTECHNOLOGY

Encoding of Qubit States in Resonators With Cat Codes

A Proof of Concept for Numerically Optimizing Encoding Pulses Using Krotov's Method

JOHAN WINTHER

Department of Microtechnology and Nanoscience
Applied Quantum Physics Laboratory
CHALMERS UNIVERSITY OF TECHNOLOGY
Göteborg, Sweden 2019

Encoding of Qubit States in Resonators With Cat Codes
A Proof of Concept for Numerically Optimizing Encoding Pulses Using Krotov's Method
JOHAN WINTHER

© JOHAN WINTHER, 2019

Supervisor: Giulia Ferrini and Simone Gasparinetti, Department of Microtechnology and Nanoscience
Examiner: Göran Johansson, Department of Microtechnology and Nanoscience

Master's thesis 2019
Department of Microtechnology and Nanoscience
Applied Quantum Physics Laboratory
Chalmers University of Technology
SE-412 96 Göteborg
Sweden
Telephone: +46 (0)31-772 1000

Cover:
Wigner function of a “cat state”.

Chalmers Reproservice
Göteborg, Sweden 2019

Encoding of Qubit States in Resonators With Cat Codes
A Proof of Concept for Numerically Optimizing Encoding Pulses Using Krotov's Method
JOHAN WINTHER
Department of Microtechnology and Nanoscience
Applied Quantum Physics Laboratory
Chalmers University of Technology

ABSTRACT

Quantum computing has gained a lot of interest in recent years and commercial products are just now entering the market. However one of the main challenges in realising a quantum computer is noise and one key technology to remedy this is quantum error correction (QEC). One way of performing QEC exploits the storage of the quantum information of a qubit in a resonator as cat codes. To do this one needs to apply encoding pulses to the coupled qubit-resonator system in order to perform a state transfer from the qubit to the resonator. These pulses need to be numerically obtained by simulation.

This thesis studies the potential of using a gradient-based optimization method, the so called Krotov's method, to numerically optimize encoding pulses for encoding arbitrary qubit states in cat codes. The Python package Krotov, a package for quantum optimal control using the method, is first used to perform state evolution from $|0\rangle$ to $|1\rangle$ and $|0\rangle$ to $|2\rangle$ of an anharmonic resonator in order to familiarise with the package and optimal control in general. It is shown that, assuming a maximum drive amplitude and no dissipation, the method can realise a $|0\rangle$ to $|1\rangle$ evolution with fidelity $F > 0.99999$ and a total pulse length of only 10.75 ns. For the $|0\rangle$ to $|2\rangle$ evolution a total pulse length of 30 ns is needed to reach the same fidelity. Finally, the Krotov is used to optimize pulses for transferring qubit states into the resonator as cat codes. The transfer of six states were simultaneously optimized in order to approximate a unitary which transfers an arbitrary qubit state into the resonator as a cat code. Using mostly experimentally realistic parameters, it is shown that the method can optimize pulses which realise the encoding of arbitrary qubit states to cat codes with a fidelity of at least $F > 0.998900$. Although plenty of challenges still remain to prove this can be done in experiments, the results points to the Krotov package as a viable tool for encoding pulse optimization.

Keywords: krotov's method, quantum optimal control, cat code, quantum computing

PREFACE

This master's thesis came to fruition when I studied the course Quantum Optics and Quantum Informatics at Chalmers University of Technology. The potential of quantum computers intrigued me and I wanted to help the progress which naturally led me to Giulia Ferrini, who became my supervisor for the project. This gave me insight into the field and I have learned a lot during the thesis. I hope that my small contribution can be used in any future endeavours.

ACKNOWLEDGEMENTS

First and foremost, I would like to thank my supervisor Giulia Ferrini for giving me the chance to pursue this project. Without her help and encouragement there would be no thesis. She helped me tremendously with the theory of quantum physics, and to navigate this complicated field, for which I am very grateful. I would also like to thank Simone Gasparinetti for helping with the project. He provided good discussion and important remarks from his experimental background, which was necessary for the work to progress. Further, I am grateful of all the helpful people at the Applied Quantum Physics Laboratory who made my time at the department enjoyable and for answering my pressing questions during the thesis work. I want to thank anyone who helped me directly or indirectly by supporting me during my studies. I wish to thank all of my friends for being with me and making all these years more than enjoyable. Lastly, I am eternally grateful for my family who have supported and always believed in me.

Johan Winther, Gothenburg, June 2019

CONTENTS

Abstract	i
Preface	iii
Acknowledgements	iii
Contents	v
1 Introduction	1
1.1 Background	1
1.1.1 Potential of Quantum Computing	1
1.1.2 Quantum Error Correction	1
1.1.3 Cat Code	1
1.1.4 Superconducting Resonators and Qubits	2
1.1.5 Cat Code Encoding Scheme	3
1.1.6 Quantum Optimal Control	3
1.2 Purpose of the Thesis	4
2 Method	5
2.1 Krotov's Method for Quantum Optimal Control	5
2.2 Krotov: the Python Package	5
2.3 Hardware and Operating System	6
3 $0\rangle \rightarrow 1\rangle$ state evolution	7
3.1 Simulation Setup	7
3.1.1 Hamiltonian	7
3.1.2 Optimization Setup	8
3.2 Results	9
3.3 Discussion	10
4 $0\rangle \rightarrow 2\rangle$ state evolution	15
4.1 Simulation Setup	15
4.1.1 Hamiltonian	15
4.1.2 Optimization Setup	15
4.2 Results	15
4.3 Discussion	16
5 Cat Code Encoding	20
5.1 Simulation Setup	20
5.1.1 Hamiltonian	20
5.1.2 Optimization Setup	21
5.2 Results	21
5.3 Discussion	22
6 Conclusions	27
6.1 Conclusive Discussion of the Use of <code>krotov</code>	27
6.2 Conclusion of Thesis	27
6.3 Future work	27
References	28

A	Appendix	30
A.1	Bloch Sphere Visualization	30
A.2	Cat Code Supplementary Figures	31
A.2.1	Wigner Function of Resonator Target States	31
A.2.2	Occupation Dynamics of Resonator During State Transfer	31
A.3	Jupyter Notebooks and Optimization Data	34

1 Introduction

The main topic of the thesis and the motivation behind it are introduced in this chapter. It starts with a presentation of the problem background in Section 1.1 followed by the purpose of the thesis in Section 1.2.

1.1 Background

In this section the problem background of the thesis is presented. First, the motivation for quantum computing will be briefly presented. Then a quick introduction to quantum error correction is given followed by the theory behind the *cat code*. After that the theory behind superconducting resonators and qubits will be reviewed in order to understand the cat code encoding scheme, where the latter will finally lead into the concept of quantum optimal control. The reader will be assumed to have basic knowledge of quantum mechanics, quantum computing and quantum optics (specifically coherent states and the Wigner function).

1.1.1 Potential of Quantum Computing

Quantum computers are thought to solve problems which are not possible with classical computers [1]. Perhaps the most famous example is using *Shor's algorithm* for prime factorization [2] which could break some public key cryptographic algorithms. Aside from quantum algorithms, there is also the prospect of using quantum computers to simulate quantum systems, which Feynman famously proposed [3] back in 1982. Since quantum systems form the basis of chemistry, particle physics and condensed matter physics, to name a few, we hope that quantum simulation can help these sciences with discoveries such as new medicine, collider dynamics and materials.

While quantum computers are starting to appear as commercial products [4], there are still a lot of challenges to be solved before large scale quantum computers can become commonplace.

1.1.2 Quantum Error Correction

One of the main challenges in building a quantum computer is combating decoherence, the process in which the quantum information of a quantum system leaks out into the environment [5]. To solve this one can perform quantum error correction (QEC). This can be done by introducing redundancy into the physical system and “spread” the quantum information to highly entangled states using quantum error correcting codes (QECC) [5]. The two prevailing methods are to either (1) encode a logical qubit into many physical qubits, or (2) encode a logical qubit into a bosonic mode in quantum harmonic resonators. Method (2) permits us to use a single physical system to store the information, which makes it a good candidate for a QECC. Leghtas, Kirchmair, Vlastakis, *et al.* [6], Mirrahimi, Leghtas, Albert, *et al.* [7] propose and Ofek, Petrenko, Heeres, *et al.* [8] demonstrate a QECC called the “cat code”, which will be the focus of this thesis. The motivation for using the cat code for QEC is that the logical basis states are eigenstates of photon-number parity, which means that the cat code requires just a single ancilla qubit in order to monitor the dominant error in the resonator (single photon loss) [8].

1.1.3 Cat Code

The logical basis states of the cat code

$$|0_L\rangle = |C_\alpha\rangle, \quad |1_L\rangle = |C_{i\alpha}\rangle \quad (1.1)$$

are built up of *cat states*: superpositions of coherent states

$$|C_\alpha\rangle = \frac{1}{\sqrt{2}}(|\alpha\rangle + |-\alpha\rangle), \quad |C_{i\alpha}\rangle = \frac{1}{\sqrt{2}}(|i\alpha\rangle + |-i\alpha\rangle). \quad (1.2)$$

That is the each basis state $|0(1)_L\rangle$ in the cat code consists of a cat state $|C_{(i)\alpha}\rangle$, which is a superposition of a coherent state $|(i)\alpha\rangle$ and its negative counterpart $|-(i)\alpha\rangle$. $|\alpha|^2$ is the mean photon number of the coherent state. The basis can also be in an odd parity where the two coherent states are subtracted instead of added, however only the even parity basis will be used in this thesis for simplicity.

These basis states can be visualized by plotting the Wigner function which is done in Figure 1.1. The characteristic features of a cat state in the Wigner plot are two lobes with interference fringes in between them [9].

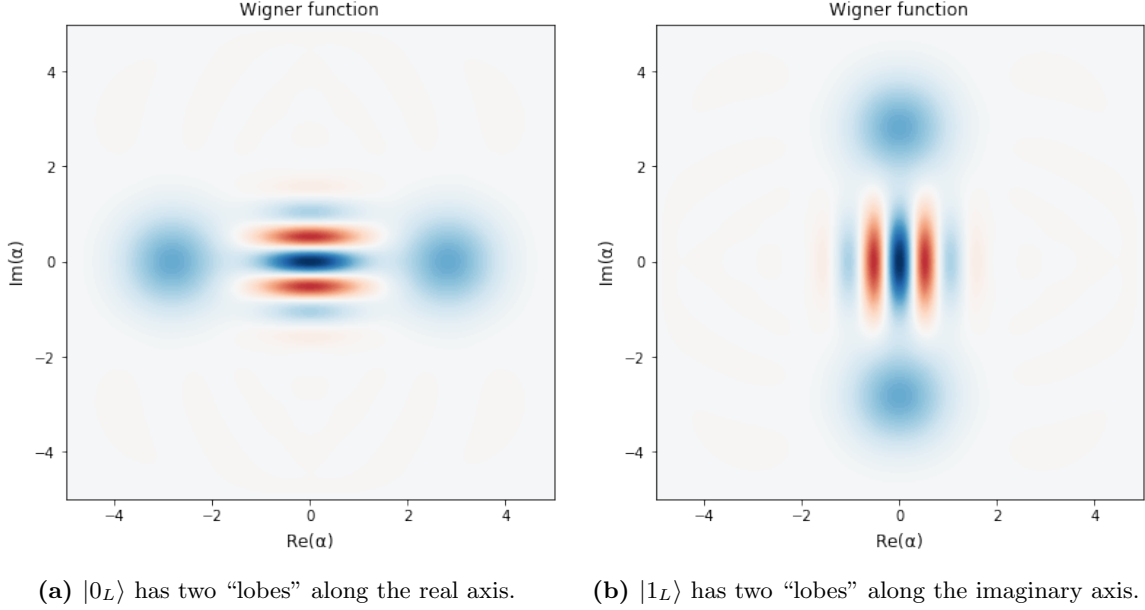


Figure 1.1: Wigner function of the cat code logical basis states with $\alpha = 2$.

Before the encoding scheme for the cat code can be explained we will quickly need to review the theory behind qubits and resonators.

1.1.4 Superconducting Resonators and Qubits

Superconducting resonators are microwave resonators. Although ideal harmonic resonators have equally spaced energy levels, in reality they are more or less anharmonic and the general Hamiltonian for a quantum anharmonic resonator is

$$\hat{H} = \omega_q \hat{a}^\dagger \hat{a} + \frac{K_q}{2} (\hat{a}^\dagger)^2 \hat{a}^2 \quad (1.3)$$

where ω is the resonance frequency, K is the anharmonic (self-Kerr) term and \hat{a} is the annihilation operator which removes an excitation from the resonator. Note that this is an approximate model as higher order terms have been neglected.

The anharmonicity can be visualised, see Figure 1.2, by plotting the eigenenergies of Equation (1.3) as a function of K . A larger anharmonicity makes the energy spacing larger for excitation states higher than $|1\rangle$. This anharmonicity allows us treat the resonator as a qubit, by only driving at the frequency specified by the energy spacing between the first two states $|0\rangle$ and $|1\rangle$. Throughout this thesis, the term “qubit” will be used to refer to an anharmonic resonator even though it has more than two energy levels. Further note, the frequency corresponding to the energy spacing between the first two levels, will be referred to as ω_q , the “resonance frequency of the qubit”.

Now if we couple a qubit to a resonator the Hamiltonian is

$$\hat{H}(t) = \underbrace{\omega_r \hat{a}^\dagger \hat{a} + \frac{K_r}{2} (\hat{a}^\dagger)^2 \hat{a}^2}_{\text{Resonator}} + \underbrace{\omega_q \hat{b}^\dagger \hat{b} + \frac{K_q}{2} (\hat{b}^\dagger)^2 \hat{b}^2}_{\text{Qubit}} + \underbrace{g(\hat{a}^\dagger \hat{b} + \hat{a} \hat{b}^\dagger)}_{\text{Coupling}}, \quad (1.4)$$

where \hat{a} and \hat{b} are the annihilation operators for the resonator and qubit respectively. There is now a coupling term with coupling strength g which means that the resonator and the qubit can exchange excitations between each other. g is assumed to be real for simplicity. This is similar to the Jaynes-Cummings Hamiltonian, but now there are added self-Kerr (anharmonicity) terms for both the qubit and the resonator. Another difference is that the Jaynes-Cummings model explicitly deals with a two-level qubit or atom, while this model has a “qubit” with arbitrary levels. Note that the rotating wave approximation has been applied to the coupling term [10].

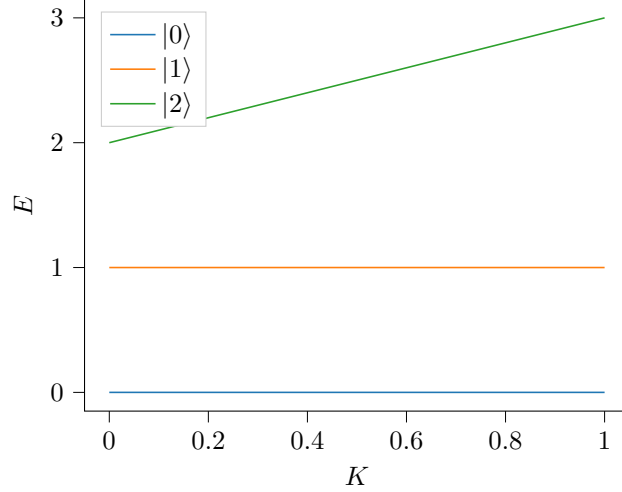


Figure 1.2: The energy levels of a three-level resonator for anharmonicity $K \in [0, 1]$ and $\omega = 1$. A resonator has $K = 1$ while a qubit has $K \neq 0$.

1.1.5 Cat Code Encoding Scheme

Now that we have an understanding of the coupled quantum system of interest we can understand how the cat code encoding scheme works. In short, the quantum information of a superconducting qubit is carefully encoded into a cavity resonator by simultaneously driving the qubit and resonator system with microwave pulses. To be specific, the unitary which we want to realise in a time T is

$$\hat{U}(T)(c_0 |0\rangle + c_1 |1\rangle) \otimes |0\rangle = |0\rangle \otimes (c_0 |C_\alpha\rangle + c_1 |C_{i\alpha}\rangle) \quad (1.5)$$

where we see that the coefficients of an arbitrary qubit state are transferred to the resonator in the cat code basis. Now the process of changing Equation (1.4) to implement the transfer in Equation (1.5) leads us to the theory of quantum optimal control.

1.1.6 Quantum Optimal Control

Quantum control is the process of controlling a quantum system by controlling the amplitude of a set of control operators [11]. Such a system can be described by a Hamiltonian of the following form [11]

$$\hat{H}(t) = \underbrace{\hat{H}_d}_{\text{Drift}} + \underbrace{u_0(t)\hat{H}_0 + \dots + u_N(t)\hat{H}_N}_{\text{Control}}, \quad (1.6)$$

where in the cat code case \hat{H}_d is the Hamiltonian in Equation (1.4). As these controls are usually electromagnetic pulses changing in time, they will be referred to as “pulse shapes” [11] in this thesis.

There are two main questions in quantum control: one of *controllability* and one of *optimal control*. The first deals with the *existence* of solutions given a Hamiltonian and the second with the *optimized* solutions for the pulse shapes $\{u_i(t)\}$ [12]. The optimal solutions are generally not analytically solvable and thus the pulse shapes need to be discretized and numerically optimized in simulation.

Ofek, Petrenko, Heeres, *et al.* numerically optimize their microwave pulse shapes using the GRAPE algorithm [13]. However, as there is no source code available for this implementation, this provides an opportunity to reproduce their result with an easy-to-use open source software package, and hopefully provide reference for future implementations.

1.2 Purpose of the Thesis

The purpose of this thesis is to, as a proof of concept, numerically optimize microwave pulses to encode the quantum information of a qubit into a resonator in cat codes. This is to provide future research with a boilerplate for performing encoding in cat codes.

The thesis is limited to

- closed quantum systems without any interaction with the environment and
- only finding pulses that *encode* the cat codes (no decoding).

2 Method

The pulses will be optimized using Krotov’s method [14], a gradient-based optimization algorithm available publicly as a ready-to-use Python package [15]. In this chapter Krotov’s method for quantum optimal control will be briefly introduced and an implementation as a Python package. Then the numerical simulations will be explained.

2.1 Krotov’s Method for Quantum Optimal Control

Krotov’s method for quantum control fundamentally relies on the variational principle to minimize a functional

$$J\left[\left\{\left|\phi_k^{(i)}(t)\right\rangle\right\},\left\{u_l^{(i)}(t)\right\}\right]$$

that depends on the pulse shapes and the quantum states of the system evolved under these pulse shapes [15]. A detailed explanation of this functional can be found in [14]. However a quick summary of how the method works will be presented here. Starting with some guess pulse shapes, the initial state is forward propagated in time using a Hamiltonian of the same form as Equation (1.6), and the value of the functional is calculated. Then changes to the pulse shapes which will decrease the value of the functional are calculated, by propagating states with these new pulse shapes, and these updates become the new pulse shapes. This continues until convergence is reached.

The underlying mathematical principles of Krotov’s method will not be addressed in the thesis, as that is outside the scope. Therefore the method will be treated as a black box function provided by the Python package which will be presented in the next section.

2.2 Krotov: the Python Package

A Python implementation of the Krotov’s method is available at [15], where an abstraction layer for doing optimizations is provided. The package will be referred to as `krotov`. The reason `krotov` was chosen is primarily because it allows for optimization of multiple objectives simultaneously. This is necessary in order to create a single encoding pulse which will realise the state transfer into the cat code basis for any arbitrary state.

The package is built on top of QuTiP, a popular software package for simulating the dynamics of quantum systems [16]. That means it can leverage all the useful features of that package, which is also another reason this method was chosen. The package provides a set of submodules which are used to setup the optimization problem. The important modules will be presented here.

The `objectives` module describes the goal of the optimization, be it a state-to-state evolution or a quantum gate. It is used to specify the initial and target states, the Hamiltonian and the initial guess pulses.

The `functionals` module provides a set of functionals which can be used for Krotov’s method. In this work the functional `chis_ss` has been chosen for all optimizations.

In the `convergence` module, help functions for the stopping criteria are provided for the optimization. It exposes values such as the overlap of the forward propagated state and target state $\langle\psi(T)|\psi^{\text{tar}}\rangle$ during the optimization which can be used to check when convergence is reached. The stopping criteria chosen for this thesis is either when a minimum fidelity is obtained, the fidelity being given by [8]

$$F = \frac{1}{S} \left| \sum_{k=1}^S \langle\psi_k(T)|\psi_k^{\text{tar}}\rangle \right|^2, \quad (2.1)$$

where S is the number of (simultaneous) state transfers we want to realise, or when the change in fidelity between iterations ΔF falls below a specified value (where a local minimum can be assumed to have been reached). The values of these will be specified in ??

Finally, the `optimization` module is used to setup the whole optimization. It is possible to choose the time discretization, convergence criteria, optimization functional, and a function which will run after every iteration. Also the step size $1/\lambda$ of the pulse updates can be chosen, which is further explained in [15]. Note however that although a large step size could achieve faster convergence, it can also lead to numerical instability.

2.3 Hardware and Operating System

All simulations and optimizations were run on a Lenovo Yoga 520-14IKB PC with an Intel(R) Core(TM) i7-8550 CPU running Windows 10. On the software side, they were run through a Jupyter notebook running Python 3.6.7 installed on Ubuntu 18.04.2 under Windows Subsystem for Linux (WSL). The source code is given in Appendix A.3.

3 $|0\rangle \rightarrow |1\rangle$ state evolution

In this simulation, the optimization was run to realise the state evolution $|0\rangle \rightarrow |1\rangle$. The pulse shape should be close to the ideal solution of a π -pulse: a gaussian pulse which performs a bit flip on a qubit. Therefore it is a suitable goal to test the method and package.

3.1 Simulation Setup

In this section the Hamiltonian and the optimization parameters will be presented.

3.1.1 Hamiltonian

The anharmonic resonator (qubit) in Equation (1.3) was chosen as it is a simple model for a physical qubit. As stated earlier such a system will be referred to as a qubit even though it has more than two energy levels. To induce transitions between the states of the qubit, control pulse terms were added to Equation (1.3), resulting in

$$\hat{H} = \omega_q \hat{a}^\dagger \hat{a} + \frac{K_q}{2} (\hat{a}^\dagger)^2 \hat{a}^2 + \Omega(t) e^{-i\omega_q t} \hat{a} + \Omega^*(t) e^{i\omega_q t} \hat{a}^\dagger, \quad (3.1)$$

where $\Omega(t)$ is the complex amplitude of the control pulse. Looking at the Hamiltonian above, it can be argued that it can be written in the form in Equation (1.6), which is needed by `krotov`, with $u_0(t) = \Omega(t) e^{i\omega_q t}$ and $u_1(t) = \Omega^*(t) e^{-i\omega_q t}$. However, there are two problems that need to be addressed. Firstly, the oscillating factors require an unnecessarily fine time discretization of the pulses. Secondly, the Krotov package expects real-valued pulse amplitudes $\{u_i(t)\}$ as inputs. The first problem was avoided by transforming the Hamiltonian into the interaction picture with respect to $\omega_q \hat{a}^\dagger \hat{a}$, also known as the rotating frame. That is the Hamiltonian is transformed with

$$\hat{U} \hat{H} \hat{U}^\dagger + i \frac{d\hat{U}}{dt} \hat{U}^\dagger, \quad (3.2)$$

where $\hat{U} = e^{-i\omega_q \hat{a}^\dagger \hat{a} t}$ which results in

$$\hat{H} \rightarrow \frac{K_q}{2} (\hat{a}^\dagger)^2 \hat{a}^2 + \Omega(t) \hat{a} + \Omega^*(t) \hat{a}^\dagger. \quad (3.3)$$

Now the pulse amplitudes $u_0(t) = \Omega(t)$ and $u_1(t) = \Omega^*(t)$, i.e. the envelope of the physical control pulse which varies significantly slower than the actual pulse. The second problem was easily fixed with a rearrangement of the terms

$$\begin{aligned} \Omega(t) \hat{a} + \Omega^*(t) \hat{a}^\dagger &= \left[\text{Re}[\Omega(t)] + i \text{Im}[\Omega(t)] \right] \hat{a} + \left[\text{Re}[\Omega(t)] - i \text{Im}[\Omega(t)] \right] \hat{a}^\dagger = \\ &= \text{Re}[\Omega(t)] (\hat{a} + \hat{a}^\dagger) + \text{Im}[\Omega(t)] i (\hat{a} - \hat{a}^\dagger). \end{aligned}$$

For intuition, $(\hat{a} + \hat{a}^\dagger)$ and $i(\hat{a} - \hat{a}^\dagger)$ correspond to rotations around the Bloch sphere¹ along the x-axis and y-axis respectively. Thus the final Hamiltonian became

$$\hat{H} = \underbrace{K_q/2 (\hat{a}^\dagger)^2 \hat{a}^2}_{\hat{H}_d} + \underbrace{\text{Re}[\Omega(t)]}_{u_0(t)} \underbrace{(\hat{a} + \hat{a}^\dagger)}_{\hat{H}_0} + \underbrace{\text{Im}[\Omega(t)]}_{u_1(t)} \underbrace{i(\hat{a} - \hat{a}^\dagger)}_{\hat{H}_1}. \quad (3.4)$$

The parameters of the qubit were chosen to model real superconducting qubits with $K_q = 2\pi \times 297$ MHz (and $\omega_q = 2\pi \times 6.2815$ GHz). The system Hamiltonian in Equation (3.4) was simulated with a truncated Hilbert space size conveniently chosen to be $N_q = 3$. A smaller truncated Hilbert space, and consequently smaller matrices, requires less computations but could possibly yield a poor approximation of the Hamiltonian. Thus the solutions of the optimization were analysed with this in mind.

¹A quick explanation of how the Bloch sphere is used for visualization is given in Appendix A.1.

3.1.2 Optimization Setup

As the long-term goal is to use this method in physical systems some constraints were added. To simulate the constraints of physical arbitrary waveform generators (AWG) a maximum sample rate of 4 GSa s^{-1} was chosen. Recall that the physical pulses oscillate at $\omega_q = 6.2815 \text{ GHz}$, a rate which 4 GSa s^{-1} can impossibly resolve. Although AWGs with higher sample rates than 4 GSa s^{-1} exist, they are expensive. However, rotating frame transformation permits the use of a relatively low rate AWG to generate the pulse envelopes $\Omega(t)$ and a high rate tone generator to create a carrier signal at ω_q , with these signals later combined in a mixer. Further, due to the noise sensitivity of superconducting systems an amplitude constraint is needed to keep the system cool enough. To set a realistic maximum amplitude A_m some derivation was required. First the maximum amplitude was chosen with the assumption that a gaussian pulse

$$g(t) = \frac{\pi/2}{\sigma\sqrt{2\pi}} e^{-\frac{1}{2}\left(\frac{t}{\sigma}\right)^2} \quad (3.5)$$

with $\sigma = 3 \text{ ns}$ can physically realise a π -rotation $|0\rangle \rightarrow |1\rangle$ in a planar transmon qubit. The problem with gaussian pulses however is that they do not go to zero at the edges. To fix this `krotov` provides a function for generating Blackman pulses. A Blackman pulse with a total length of 6σ is a good approximation of a Gaussian pulse, with the added benefit of going to zero at the edges. However, due to the approximation, the integral of the Blackman pulse will not exactly be equal to the integral of the corresponding gaussian pulse, which is needed to realise the π -rotation. This can be fixed by using a prefactor C which can be calculated by solving

$$C \int_0^{6\sigma} \frac{1}{\sqrt{2\pi}\sigma} B(t) dt = \int_0^{6\sigma} g(t - 3\sigma) dt \quad (3.6)$$

where $B(t)$ is the Blackman pulse. This is now used to determine the maximum amplitude

$$A(\sigma) = \frac{C}{\max(\sigma, 3)\sqrt{2\pi}} \quad (3.7)$$

with $A_m = A(\sigma = 3)$. This amplitude constraint is enforced by calling a function after every iteration which limits all pulse shape values $|\Omega| < A_m$. Conveniently, the Blackman pulse was also used as the initial guess pulse with $u_0(t) = A(T/6)B(t)$, $u_1(t) = 0$.

Another constraint was added so that the edges of the pulses were always zero. This was done with a switch-on/switch-off of 2 ns . This ramp shape is half a Blackman pulse and is provided by `krotov`'s `flattop` function.

For the $|0\rangle \rightarrow |1\rangle$ state evolution, pulse shapes were optimized with varying lengths from 4.25 ns to 30 ns with convergence criteria $F > 0.99999$ or $\Delta F < 10^{-7}$. The step size was chosen as $\lambda = \frac{1}{\frac{1}{2}A_m}$. The reason for optimizing for various pulse lengths was that faster pulse changes gives a broader support in the frequency spectrum which can ultimately induce transitions in other levels. Therefore the optimization needs to find a solution which circumvents this problem.

3.2 Results

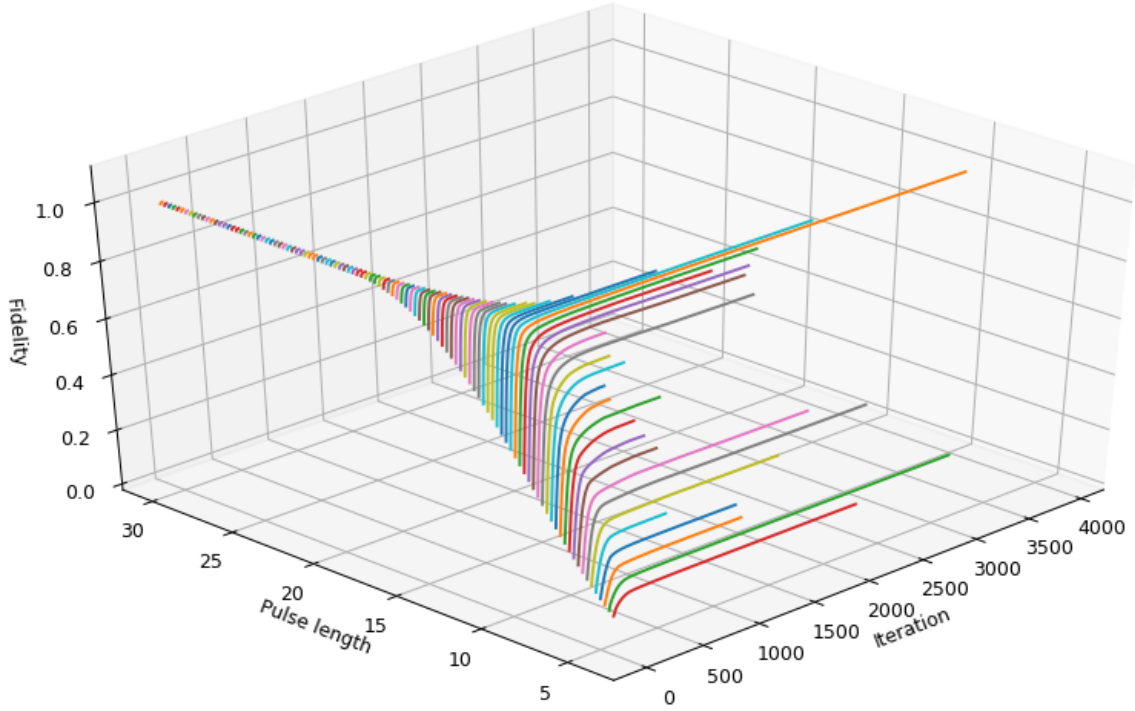


Figure 3.1: Fidelity during optimizations for every pulse length (ns). The different colors help distinguish the lines.

In Figure 3.1 the fidelity during all optimizations (with pulse lengths from 4.25 ns to 30 ns) are plotted. The “starting fidelity” is the fidelity which is obtained with the guess pulses while the “optimized fidelity” is the fidelity obtained with the optimized pulses. For pulse lengths longer than 15 ns the fidelity starts at values close to the goal ($F > 0.9$) and the number of iterations is relatively low (less than 85 iterations). In contrast, pulses shorter than 15 ns start at lower fidelities while the number of iterations are roughly one order of magnitude larger with no clear pattern with respect to the pulse length.

To give a more detailed picture, the starting fidelity and optimized fidelity are plotted over pulse length in Figure 3.2. The optimizations where the fidelity goal was not reached, pulse lengths equal to and below 10.50 ns, are marked with stars.

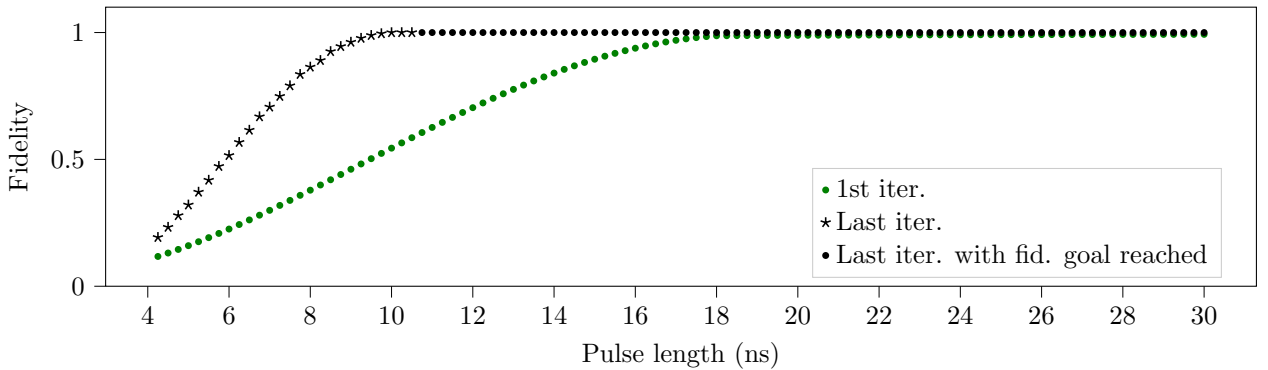


Figure 3.2: Starting fidelity (green) and optimized fidelity (black) of pulse lengths from 4.25 ns to 30 ns.

Further analysis is done on pulses with lengths 4.25 ns, 6.0 ns, 8.0 ns, 10.0 ns, 20.0 ns and 30.0 ns. The optimized pulse shapes $\text{Re}(\Omega)$ and $\text{Im}(\Omega)$ are plotted in Figure 3.3 together with the guess pulses. Pulses longer than 20 ns require only fine adjustments to the Blackman guess pulse while shorter pulses have an imaginary

part which is maximized for the whole duration of the pulse. In order to gain insight into the shape of the pulse solution, we analyse its spectral content by performing a Fourier analysis.

The spectrum of the control pulse $\Omega(t)$ in the lab frame ($\Omega(t)e^{i\omega_q t}$) is shown in Figure 3.4. For all pulse lengths there is a peak centered roughly at ω_q with a quickly decaying end in positive direction (towards $\omega_q + K_q$). Following the trend, it can be observed that the width of the peak becomes narrower for longer pulses. For the highest pulse length 30 ns there is almost no support at $\omega_q + K_q$ nor $\omega_q - K_q$.

The time evolution of the system under the optimized pulses are visualized by plotting the occupation of the states over time, Figure 3.5, and the projection of the state on the Bloch sphere over time, Figure 3.6.

For short pulse lengths there is not enough time for the evolution from $|0\rangle$ to $|1\rangle$, but for a pulse length of roughly 10.0 ns the goal is reached. Figure 3.5 (b) shows a little rise in occupation of $|2\rangle$ around 7.5 ns. From the Bloch sphere visualization it appears that shorter pulse lengths lead to deviations from the pure y-axis rotation. This can be clearly seen in Figure 3.6 (d) for a pulse length of 10 ns, where the fidelity goal was reached but short enough that the maximum amplitude is reached for the guess pulse.

3.3 Discussion

As the system was set up to realise a π -rotation for a Blackman pulse with length $T = 6\sigma = 6 \times 3 \text{ ns} = 18 \text{ ns}$, it is no surprise that the starting fidelity is almost unity down to pulse lengths of 18 ns. Shorter than that, the amplitude constraint affects the starting pulse; as it becomes shorter the amplitude is maximised. This explains the drop in starting fidelity all the way down to 4.25 ns. Further, for pulse lengths shorter than 10.75 ns the optimization cannot reach the fidelity goal of $F > 0.99999$ which is expected as the amplitude constraint means that there just is not enough time to realise the state transfer. This is supported by the fact that the imaginary part is maximised for pulse lengths shorter than 10.75 ns. It can be assumed that the optimization is trying to compensate for the shorter pulse time.

One possible reason for the fluctuations in the number of iterations for the pulse lengths which did not reach the fidelity goal is that the steepness around the (assumed) local minima could differ significantly for different pulse lengths. This is very much in contrast with the low and steady number of iterations needed when the fidelity goal is reached. Even though the increase in pulse length should increase the number of possible solutions, increasing the chance of reaching the fidelity goal, the fast convergence is most probably due to the fact that the initial guess pulse brings the state close to the target. One might consider exploring this solution space, however it could potentially be infinite in size. For the purpose of realising the defined state evolution, this is not needed in practice as any solution which realises the transfer should be good enough.

With the previous statements in mind, the fact that the solutions found for pulse lengths shorter than 18 ns show a small increase in the $|2\rangle$ population after the population inversion could point to a need to penalize this state. That is because if the state is too occupied during the transfer one cannot be sure that the states above that will remain unoccupied. This hypothesis could be checked by simulating the system using the optimized pulses, but with a larger truncated Hilbert space. If the final state reaches the target, the truncation is a good approximation. `krotov` suggests to add dissipation to the states which should be penalized as there is currently no support for state-dependent constraints. However this also increases the computation time as the Hamiltonian needs to either be expressed as a Liouvillian or propagated with collapse terms in the master equation. We therefore leave this analysis for future studies.

The spectrum of the pulse shapes somewhat explains the “strategy” of the optimization. For the long pulse lengths there is no problem in keeping the pulse frequency mostly around the first transition frequency, only driving the qubit to $|1\rangle$. As the pulses become shorter the peak becomes wider, but the solutions try to keep the amplitude at the second transition frequency $\omega_r + K_q$ low to prevent the qubit from going into $|2\rangle$. Eventually, for short enough pulses this level becomes a little bit occupied which can be seen in Figure 4.5, but then drops to zero. Perhaps the solution tries to “take a shortcut” through $|2\rangle$, which may be a viable strategy, but if that is the case then one needs to set $N_q = 4$ and penalize $|3\rangle$ to make sure that the truncation is a valid approximation.

In conclusion, `krotov` has no problem finding a solution to this simple state transformation.

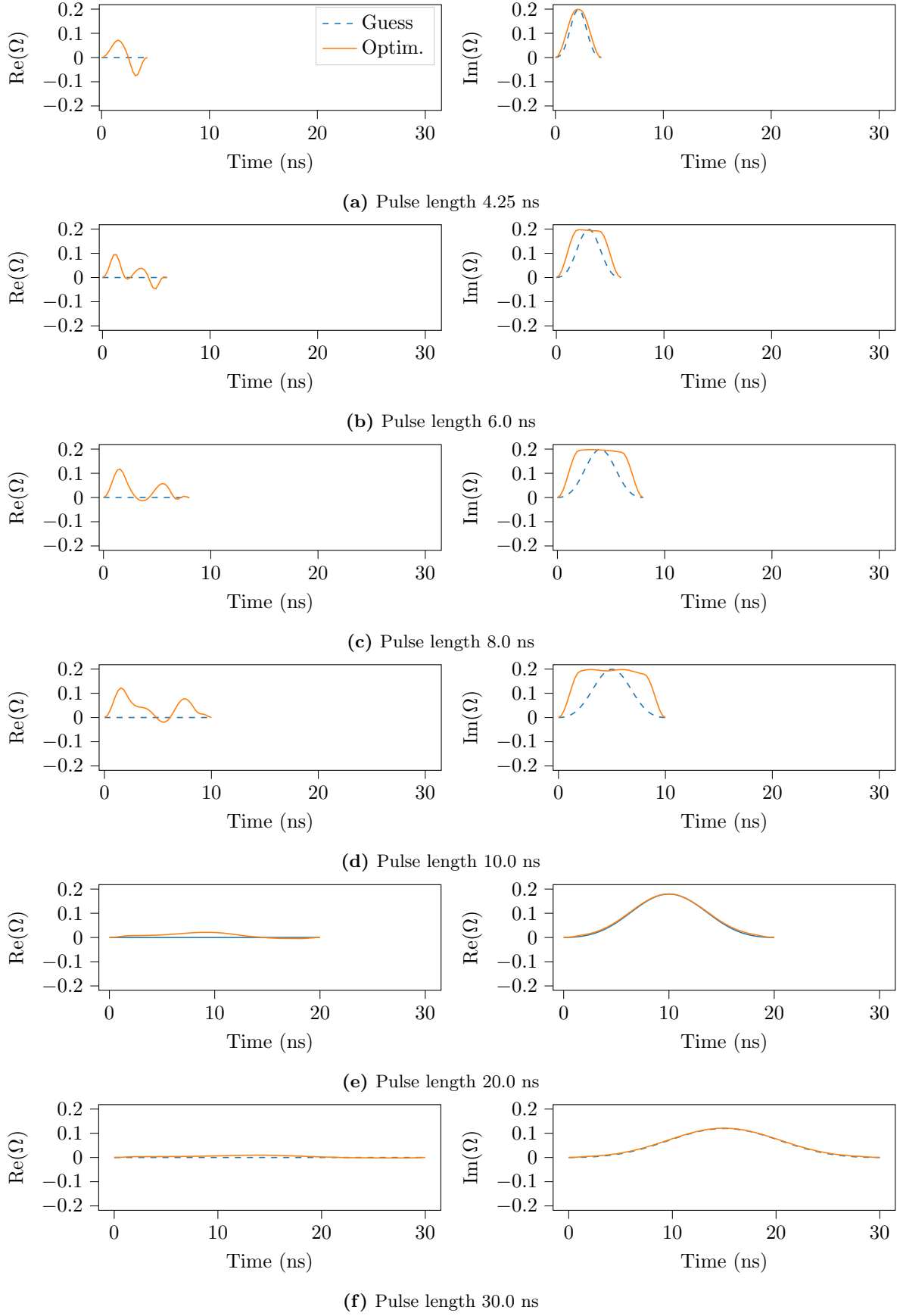


Figure 3.3: Optimised pulse shapes and guess pulses (dashed) for pulse lengths (a) 4.25 ns, (b) 6.0 ns, (c) 8.0 ns, (d) 10.0 ns, (e) 20.0 ns, and (f) 30.0 ns. Short pulses (<10 ns) change substantially from the starting Blackman shape while long pulses (>20 ns) only require fine adjustments.

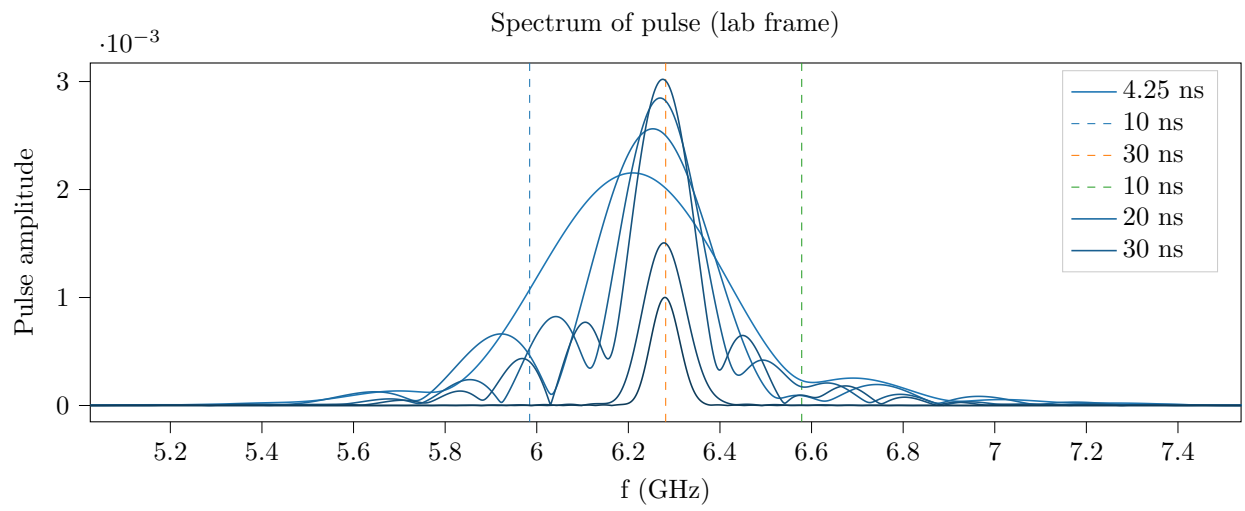
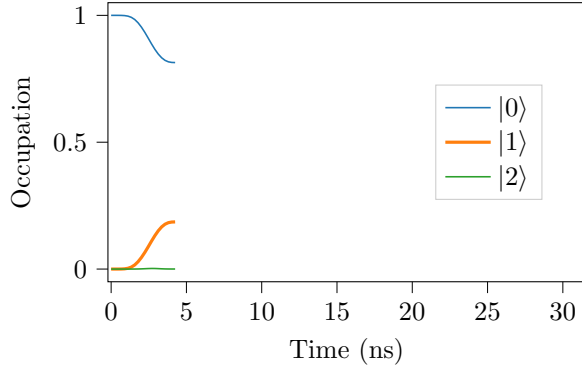
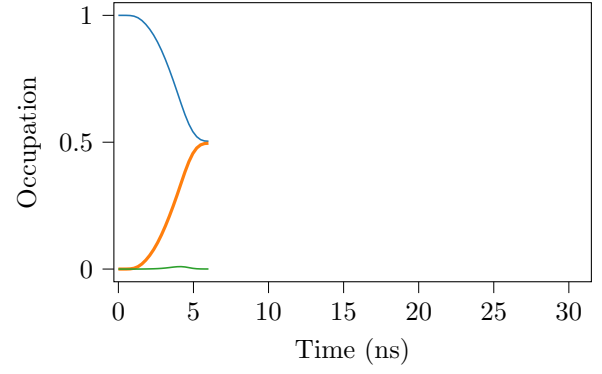


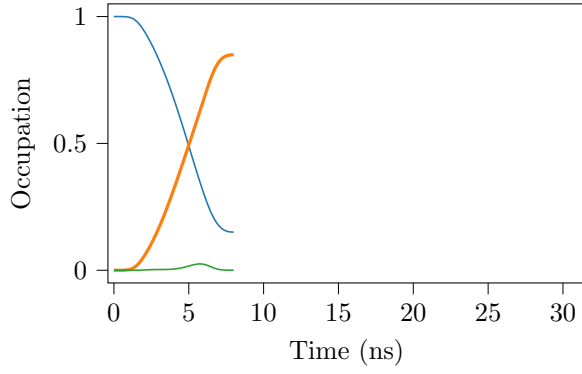
Figure 3.4: Frequency spectrum of the complex pulses in Figure 3.3. The vertical lines indicate (from left to right) $\omega_q - K_q$, ω_q , $\omega_q + K_q$ (all divided by 2π).



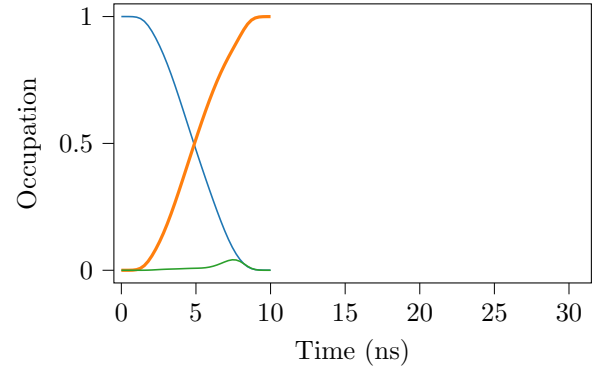
(a) Pulse length 4.25 ns



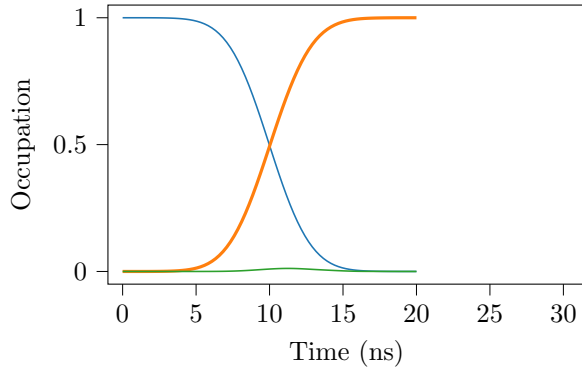
(b) Pulse length 6.0 ns



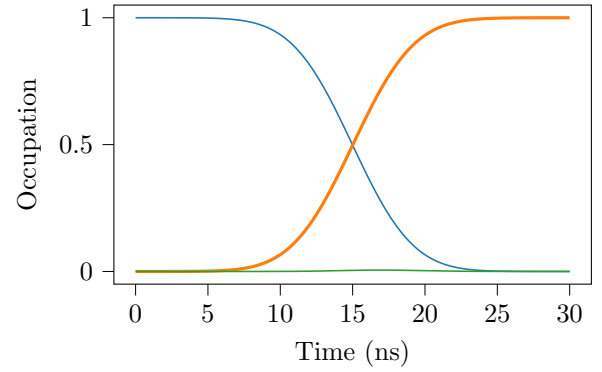
(c) Pulse length 8.0 ns



(d) Pulse length 10.0 ns

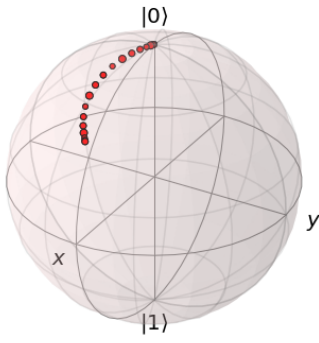


(e) Pulse length 20.0 ns

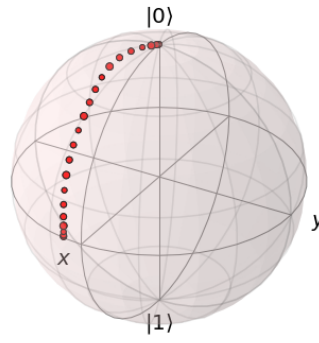


(f) Pulse length 30.0 ns

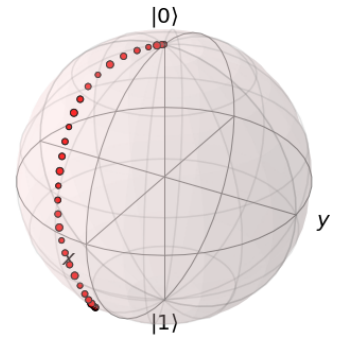
Figure 3.5: Energy level occupation over time during the $|0\rangle \rightarrow |1\rangle$ evolution for different lengths of optimized pulses.



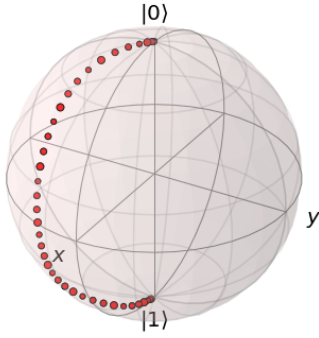
(a) Pulse length 4.25 ns



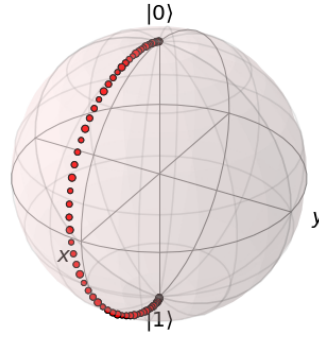
(b) Pulse length 6.0 ns



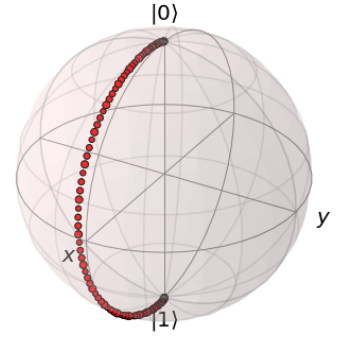
(c) Pulse length 8.0 ns



(d) Pulse length 10.0 ns



(e) Pulse length 20.0 ns



(f) Pulse length 30.0 ns

Figure 3.6: Time dynamics on the Bloch sphere for different lengths of optimized pulses.

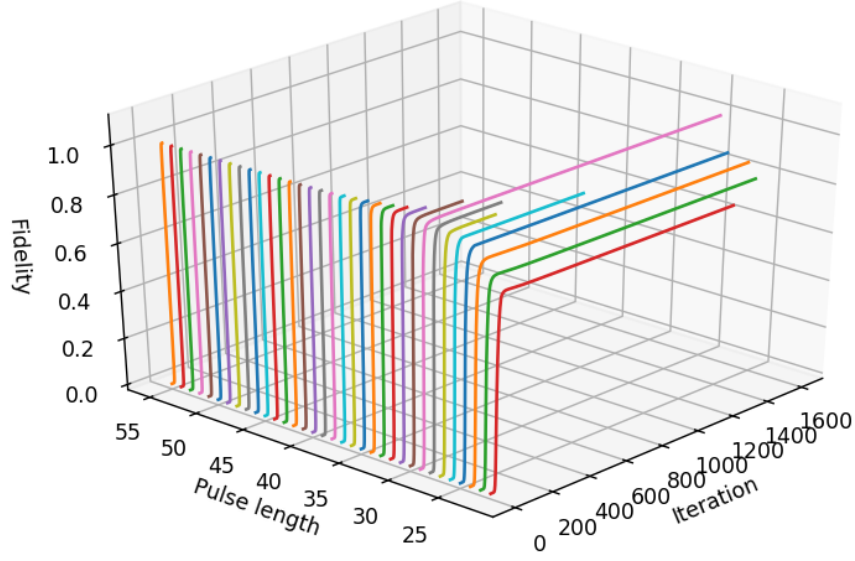


Figure 4.1: Fidelity during optimizations for every pulse length (ns).

4 $|0\rangle \rightarrow |2\rangle$ state evolution

In this simulation, the optimization was run to realise the state evolution $|0\rangle \rightarrow |2\rangle$. The pulse shape is non-trivial, therefore it is another suitable goal to test the method.

4.1 Simulation Setup

In this section the Hamiltonian and the optimization parameters will be presented.

4.1.1 Hamiltonian

The same Hamiltonian as the $|0\rangle \rightarrow |1\rangle$ evolution was used (Equation (3.1)) with the same truncation.

4.1.2 Optimization Setup

Pulse shapes were optimized with varying lengths from 22 ns to 30 ns with convergence criteria $F > 0.99999$ or $\Delta F < 10^{-9}$. The low ΔF was needed because the changes were very small in the beginning of the optimization. The step size was chosen as $\lambda = \frac{1}{2A_m}$ due to slow convergence. In contrast to the $|0\rangle \rightarrow |1\rangle$ state evolution both initial guess pulses were chosen to be Blackman pulses $u_0(t) = u_1(t) = A(T/6)B(T)$.

4.2 Results

Once again all optimization runs are shown in Figure 4.1. All runs start at almost zero fidelity while pulse lengths longer than 30 ns reach the fidelity goal of $F > 0.99999$. The number of iterations is relatively low for pulses longer than 30 ns while for shorter pulses the iterations fluctuate. Note that for pulse lengths shorter than 22 ns the optimization stopped after the first iteration due to $\Delta F < 10^{-9}$, therefore those results have been omitted.

In Figure 4.2 the fidelity is shown with respect to the pulse length and it is seen that the fidelity goal is reached for pulses longer than and including 30 ns.

The optimized pulses are shown in Figure 4.3. For all pulse lengths the pulses have roughly the same shape, with a quick rise and a short plateau, then oscillations until the end. The longest pulse at 55 ns has more oscillations than shorter ones, but instead they are lower in amplitude. To get some insight, the frequency

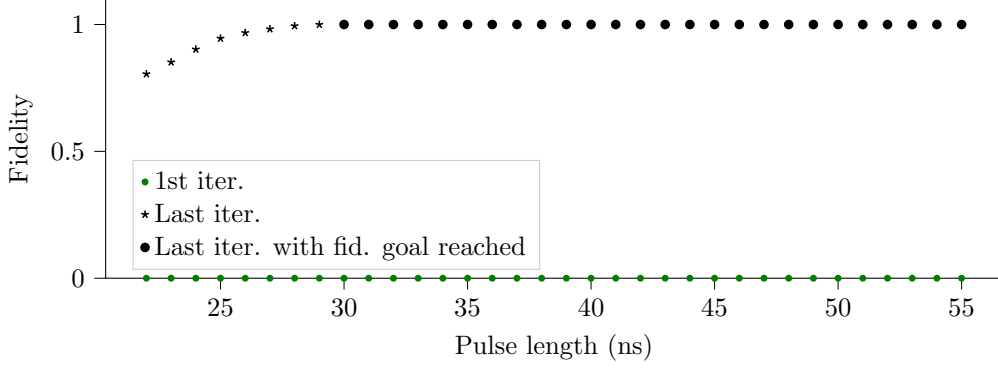


Figure 4.2: Starting fidelity (green) and optimized fidelity (black) of pulse lengths from 22 ns to 55 ns.

spectrum, Figure 4.4, shows large support at ω_q and $\omega_q + K_q$. For longer pulses, the peak at $\omega_q - K_q$ disappears. Just as the previous state evolution, the peaks narrow for longer pulse lengths.

The occupation dynamics in Figure 4.5 show a slow oscillation for all pulse lengths for all states. Further, the occupation probability of $|1\rangle$ rises to about 0.75 until the middle-point of the pulse and then falls to zero in the end, while $|2\rangle$ starts to rise at the point of the population inversion. For the shorter pulse lengths it can be seen that there isn't enough time to realise the evolution.

4.3 Discussion

The “strategy” for all pulse lengths in this case is to first invert the population and then at the halfway point start simultaneously driving the second transition level to start pumping to $|2\rangle$. The pulse shapes also reflects this as the oscillation that starts after the plateau has a frequency of K_q , which is also visible in the frequency spectrum. While the peak at $\omega_q + K_q$ was expected, the peak at $\omega_q - K_q$ for pulse lengths shorter than 29 ns is a surprise with no clear explanation. It is also not clear why the solutions drive harder at this frequency the shorter the pulse length.

For this optimization the initial guess pulses were very far from any solution, with the fidelity almost starting at zero for all pulse lengths. The fidelity goal $F > 0.99999$ was reached down to $T = 30$ ns, which is slightly longer than the $|0\rangle \rightarrow |1\rangle$ evolution. Looking at the occupation dynamics and pulse shapes could give hints as to why this is the case. One reason could be that there needs to be enough periods of oscillations to drive to $|2\rangle$, which is not the case for the $|0\rangle \rightarrow |1\rangle$ evolution where the integral of the pulse shape is of importance. Further, it appears that the fidelity drops in the same way as for the $|0\rangle \rightarrow |1\rangle$ evolution for shorter pulse lengths. However we cannot draw any conclusions for pulse lengths shorter than 22 ns. Perhaps with a low ΔF one might reach a solution that follows the trend, but this is only speculation.

The number of iterations also fluctuates for pulse lengths which do not reach the fidelity goal, just as for the $|0\rangle \rightarrow |1\rangle$ evolution.

Interestingly, for both transfers the optimization converges quickly to a relatively high fidelity, while the majority of the time is spent fine-tuning the pulse shapes. This could be a side-effect of the static step size, which could be dynamically changed for faster convergence.

To conclude, `krotov` can also be successfully used to optimize for somewhat more complicated transfers than the simple qubit rotation.

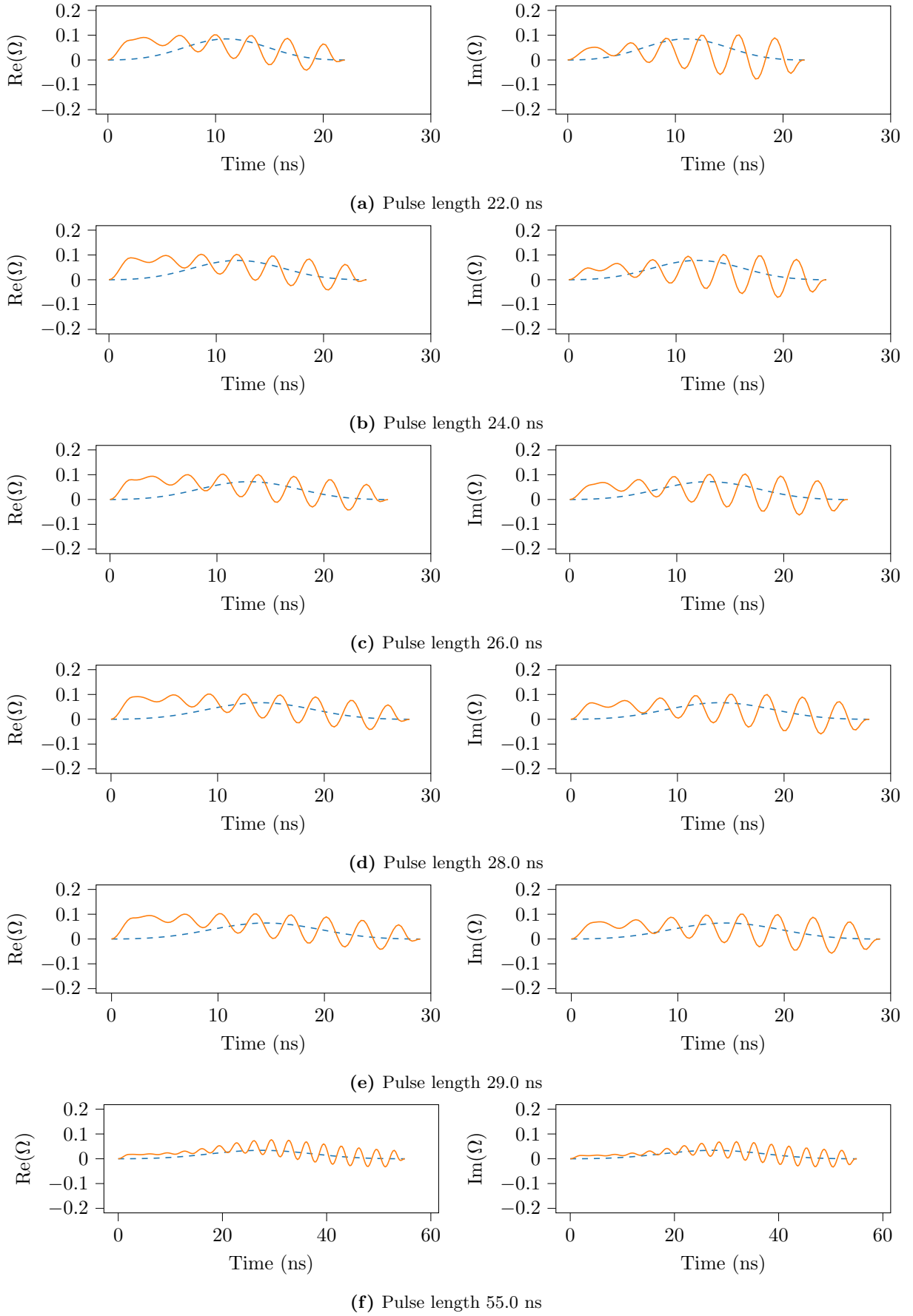


Figure 4.3: Optimised pulse shapes and guess pulses (dashed) for pulse lengths (a) 22 ns, (b) 24 ns, (c) 26 ns, (d) 28 ns, (e) 29 ns, and (f) 55 ns. Oscillations appear in all solutions.

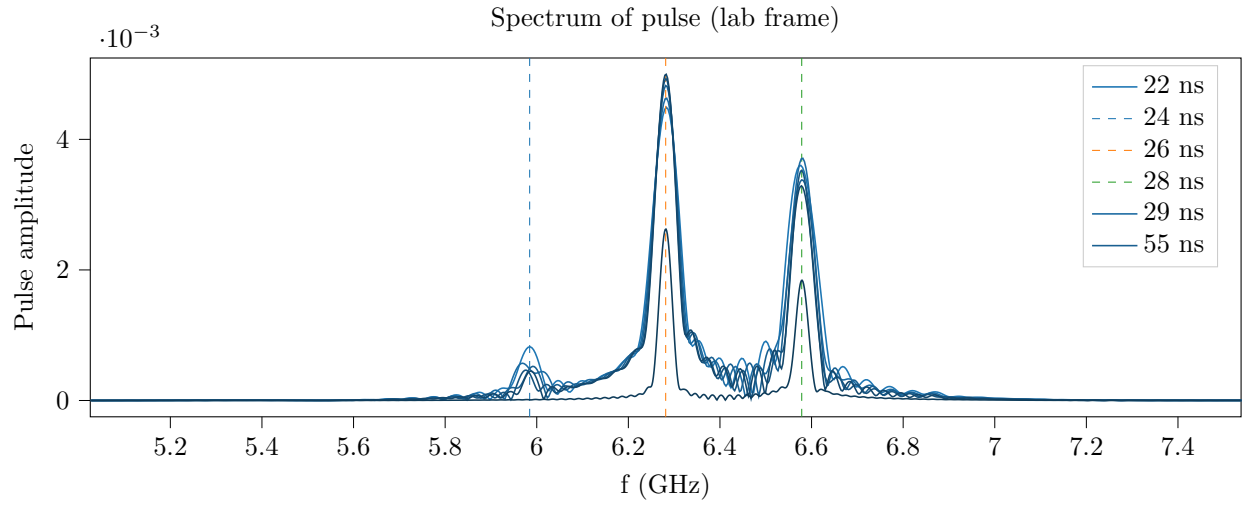
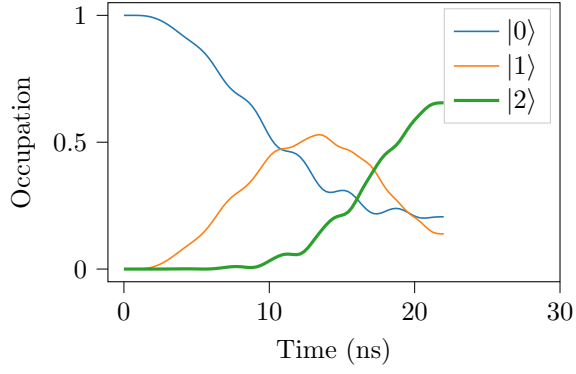
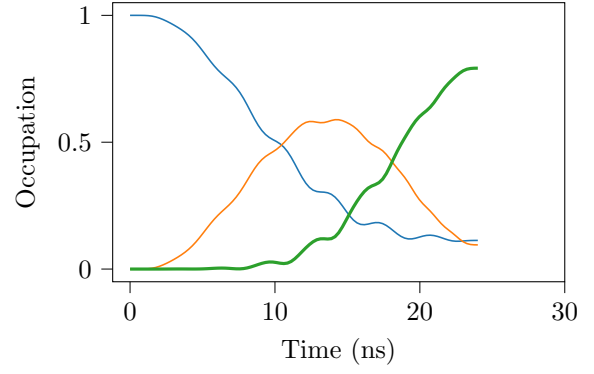


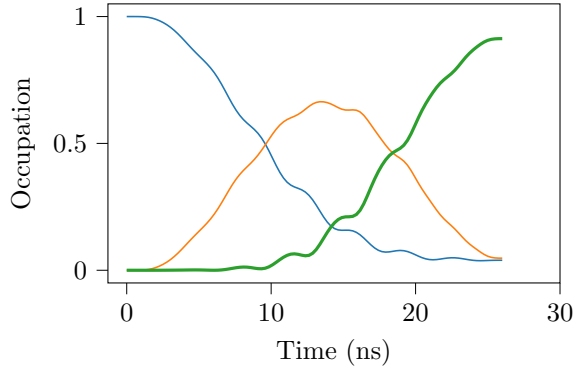
Figure 4.4: Frequency spectrum of the complex pulses in Figure 4.3. The vertical lines indicate (from left to right) $\omega_q - K_q$, ω_q , $\omega_q + K_q$ (all divided by 2π).



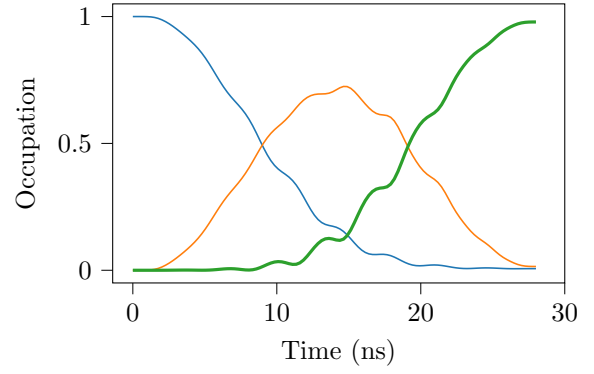
(a) Pulse length 22.0 ns



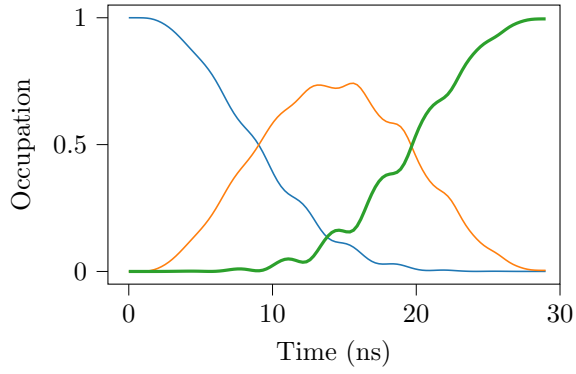
(b) Pulse length 24.0 ns



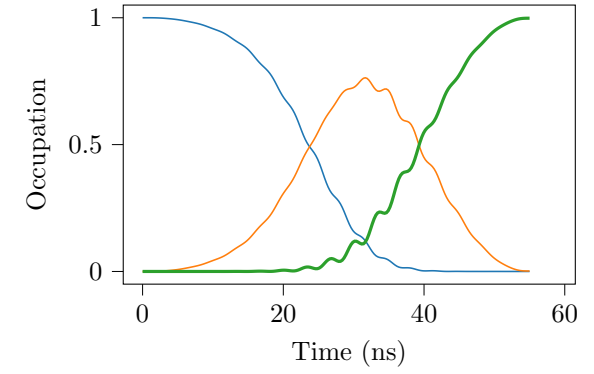
(c) Pulse length 26.0 ns



(d) Pulse length 28.0 ns



(e) Pulse length 29.0 ns



(f) Pulse length 55.0 ns

Figure 4.5: Energy level occupation over time during the $|0\rangle \rightarrow |2\rangle$ evolution for different lengths of optimized pulses.

5 Cat Code Encoding

For the cat code encoding, six simultaneous objectives were chosen to give encoding pulses which maps the six “cardinal” qubit states on the Bloch sphere to the corresponding cat code states in the resonator. These initial qubit states are

$$\begin{aligned} &|0\rangle, |1\rangle, \\ &\frac{|0\rangle + |1\rangle}{\sqrt{2}}, \frac{|0\rangle - |1\rangle}{\sqrt{2}}, \\ &\frac{|0\rangle + i|1\rangle}{\sqrt{2}}, \frac{|0\rangle - i|1\rangle}{\sqrt{2}} \end{aligned}$$

with target state $|0\rangle$. The resonator initial state is $|0\rangle$ (in the Fock basis) and the corresponding target states are

$$\begin{aligned} &|C_\alpha\rangle, |C_{i\alpha}\rangle, \\ &\frac{|C_\alpha\rangle + |C_{i\alpha}\rangle}{\sqrt{2}}, \frac{|C_\alpha\rangle - |C_{i\alpha}\rangle}{\sqrt{2}}, \\ &\frac{|C_\alpha\rangle + i|C_{i\alpha}\rangle}{\sqrt{2}}, \frac{|C_\alpha\rangle - i|C_{i\alpha}\rangle}{\sqrt{2}}. \end{aligned}$$

The hope is that by optimizing these six states the pulse shapes will approximate the unitary in Equation (1.5).

5.1 Simulation Setup

In this section the Hamiltonian and the optimization parameters will be presented.

5.1.1 Hamiltonian

In this simulation the coupled qubit-resonator system in Equation (1.4) was used. As the operators \hat{a} and \hat{b} commute, the rewriting used in Equation (3.4) was also used for the resonator. The rotating frame transformation is done here with respect to $\omega_r \hat{a}^\dagger \hat{a} + \omega_q \hat{b}^\dagger \hat{b}$. However, as the coupling term has no time dependence and does not commute with the operators $\hat{a}^\dagger \hat{a}$ and $\hat{b}^\dagger \hat{b}$ there will still be a time dependence in the rotating frame

$$g(\hat{a}\hat{b}^\dagger + \hat{a}^\dagger \hat{b}) \rightarrow g(\hat{a}\hat{b}^\dagger e^{i(\omega_q - \omega_r)t} + \hat{a}^\dagger \hat{b} e^{-i(\omega_q - \omega_r)t}). \quad (5.1)$$

This was a problem because **krotov** expects \hat{H}_d to be time independent. There is a way to “simulate” the coupling term (5.1) by inserting it as an external time dependent pulse, and omitting it from optimization, which was done in this case. The coupling term was then split into a real and imaginary part which is, as stated before, required by **krotov**.

The final Hamiltonian provided to **krotov** was then

$$\begin{aligned} \hat{H} = & \underbrace{K_r/2(\hat{a}^\dagger)^2 \hat{a}^2 + K_q/2(\hat{b}^\dagger \hat{b})^2}_{\hat{H}_d} + \\ & + \underbrace{\text{Re}[\Omega_r(t)](\hat{a} + \hat{a}^\dagger)}_{u_0(t)} + \underbrace{\text{Im}[\Omega_r(t)]i(\hat{a} - \hat{a}^\dagger)}_{\hat{H}_0} + \underbrace{\text{Re}[\Omega_q(t)](\hat{b} + \hat{b}^\dagger)}_{u_1(t)} + \underbrace{\text{Im}[\Omega_q(t)]i(\hat{b} - \hat{b}^\dagger)}_{\hat{H}_1} + \underbrace{\text{Re}[\Omega_q(t)](\hat{b} + \hat{b}^\dagger)}_{u_2(t)} + \underbrace{\text{Im}[\Omega_q(t)]i(\hat{b} - \hat{b}^\dagger)}_{\hat{H}_2} + \underbrace{\text{Re}[\Omega_q(t)](\hat{b} + \hat{b}^\dagger)}_{u_3(t)} + \underbrace{\text{Im}[\Omega_q(t)]i(\hat{b} - \hat{b}^\dagger)}_{\hat{H}_3} \\ & + \underbrace{\cos((\omega_q - \omega_r)t)}_{u_4(t)} \underbrace{g(\hat{a}\hat{b}^\dagger + \hat{a}^\dagger \hat{b})}_{\hat{H}_4} + \underbrace{\sin((\omega_q - \omega_r)t)}_{u_5(t)} \underbrace{ig(\hat{a}\hat{b}^\dagger - \hat{a}^\dagger \hat{b})}_{\hat{H}_5} \end{aligned} \quad (5.2)$$

The parameters of this system are presented in Table 5.1. These were chosen to resemble the physical values measured in [8], except for g which was chosen at relatively large value to reduce the pulse length needed to realise the transfer.

Table 5.1: Hamiltonian parameters

Param.	Value
$\omega_q/(2\pi)$	6.2815 GHz
$K_q/(2\pi)$	297 MHz
$\omega_r/(2\pi)$	8.3056 GHz
$K_r/(2\pi)$	4.5 kHz
$g/(2\pi)$	0.225 GHz

The truncated Hilbert space size for the resonator was chosen to be $N_r = 8$ with the mean photon number $\alpha = 2$. Due to the large system size, the qubit's truncated Hilbert space size was set to $N_q = 2$.

5.1.2 Optimization Setup

The optimization was setup in the same way as the previous simulation, however due to the rapid oscillations at $|\omega_q - \omega_r|$ (due to the coupling pulse) a finer time discretization of 24 GSa s^{-1} was chosen. The step size was chosen as $\lambda = \frac{1}{\frac{1}{2}A_m}$ and the pulse length $T = 60 \text{ ns}$ to allow the coupling to affect the system. Further, convergence criteria was chosen as $F > 0.999999$ or $\Delta F < 10^{-6}$. Another important step in optimizing in the rotating frame was to convert the target states into the rotating frame in order for the final states to be correct in the lab frame. Initial guess pulses were chosen to be the same Blackman pulses in the setup for the $|0\rangle \rightarrow |2\rangle$ evolution.

5.2 Results

We now present the main results of this thesis: the optimization of pulses for encoding a cat state in a resonator from a coupled qubit. The cat encoding optimization reached the convergence criteria of $\Delta F < 10^{-6}$ after 2389 iterations (corresponding to roughly 41 hours and 28 minutes) with a fidelity $F = 0.999234$, (recall the fidelity measure for multiple objectives in Equation (2.1)). The individual fidelities for the 6 initial states are shown in Table 5.2, where we can see that all individual fidelities are above 0.999000.

Table 5.2: Fidelities for the individual state transfers (ordered from highest to lowest).

State	F
$(0\rangle + i 1\rangle)/\sqrt{2}$	0.99939453
$(0\rangle - 1\rangle)/\sqrt{2}$	0.99932348
$(0\rangle + 1\rangle)/\sqrt{2}$	0.99930147
$ 0\rangle$	0.99920509
$ 1\rangle$	0.99918837
$(0\rangle - i 1\rangle)/\sqrt{2}$	0.99899637

To corroborate how well the qubit was mapped to the cat code basis, multiple states spread around the Bloch sphere were transferred with the pulse solution. The corresponding fidelities are shown on the Bloch sphere in Figure 5.1, where we can see an asymmetry with larger fidelities toward $(|0\rangle + i|1\rangle)/\sqrt{2}$. All in all the minimum fidelity among all of the transferred states is 0.998996.

The pulse shapes of the qubit and resonator are shown in Figure 5.2. Comparing the resonator and qubit, we can see that the resonator pulse has rapid oscillations throughout the whole pulse while the qubit exhibits some small quick oscillation at sparse times. The spectrum of the pulse is shown in Figure 5.3 and gives us some insight into the pulse shapes. The qubit control pulse shows a wide peak at ω_q , two small peaks at ω_r and $2\omega_r - \omega_q$ and two barely noticable peaks at $\frac{1}{4}\omega_r$ and $\frac{1}{2}\omega_r$. The resonator pulse has one wide peak at ω_r , a smaller one at ω_q and an even smaller peak at $2\omega_r - \omega_q$.

The dynamics of the qubit is shown in Figure 5.4 for all state transfers. Here we see that there is always a rapid oscillation present in the occupation probability. Looking at the dynamical behaviour one can see that common for all transfers is for the qubit to stay somewhat close to an equal superposition between $|0\rangle$ and $|1\rangle$ and then at circa 50 ns evolve to $|0\rangle$.

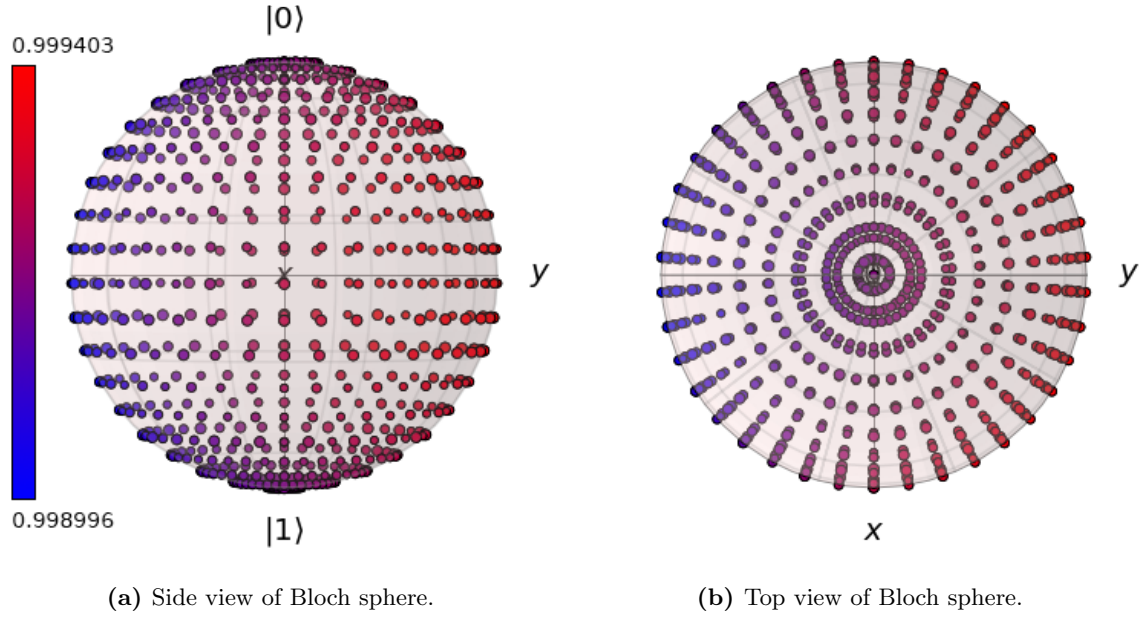


Figure 5.1: The fidelities of every simulated state transfer shown on the Bloch sphere. There is an asymmetry in the fidelity with higher fidelity towards the state $(|0\rangle + i|1\rangle)/\sqrt{2}$.

One interesting measure we can look at is the maximum occupation of the 8 resonator states, to which the resonator Hilbert space was truncated. This can give us information about the validity of the Hilbert space truncation. In Figure 5.5 the maximum reached occupation probability are plotted for all states. This is done for all the 6 state transfers. Looking only at the odd states there is a clear downward trend for higher states, with $|7\rangle$ only reaching circa 0.2 of occupation probability during the $|0\rangle$ transfer. $|6\rangle$ is in the 0.2–0.3 occupation range for all transfers. This shows that the chosen truncation is appropriate, but ideally a somewhat larger space should be used. The dynamics of the resonator level occupation are provided in Appendix A.2.2 for further analysis.

Finally, we can plot the Wigner function of the final resonator states, and compare it with the target states. This is done in Figure 5.6 where the final states have been transformed back into the lab frame. As is evident from the plots they are close to the target states shown in Figure A.2.

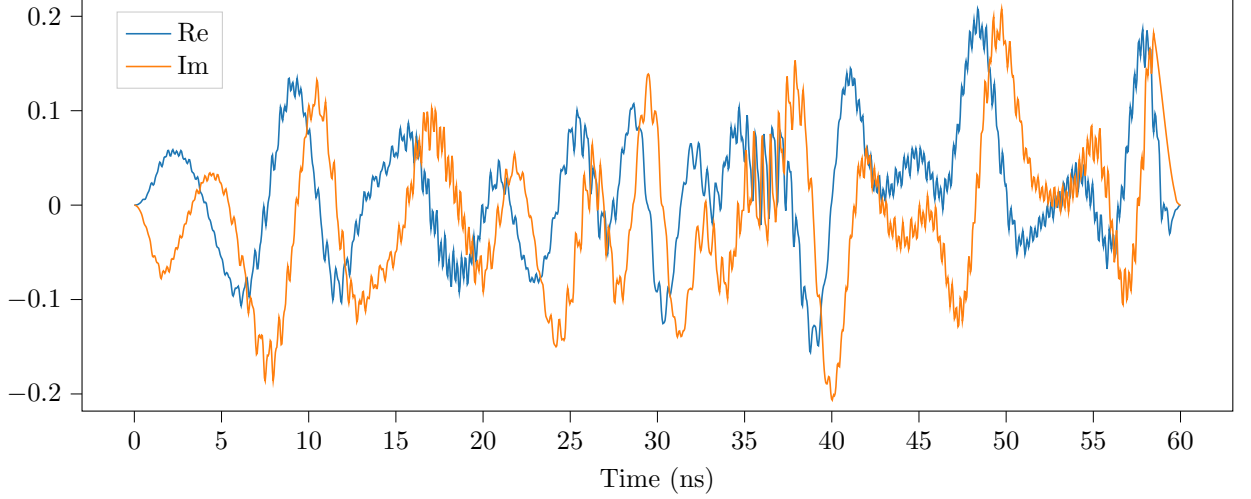
5.3 Discussion

The six simultaneous objective optimization ended with a total fidelity of $F = 0.999234$ and the individual fidelities all over 0.9989000. The simulations also showed that the transfers of states evenly spread around the Bloch sphere all had a minimal fidelity above 0.9989000 for the transferred states. This supports the validity of the method as a mean to obtain one pulse to encode all six states. There is no clear reason for why there is a bias in the fidelities for states closer to $(|0\rangle + i|1\rangle)/\sqrt{2}$. One reason could be that the guess pulses introduce a bias and this bias is still left if the convergence is due to ΔF . Another reason could be due to numerical errors.

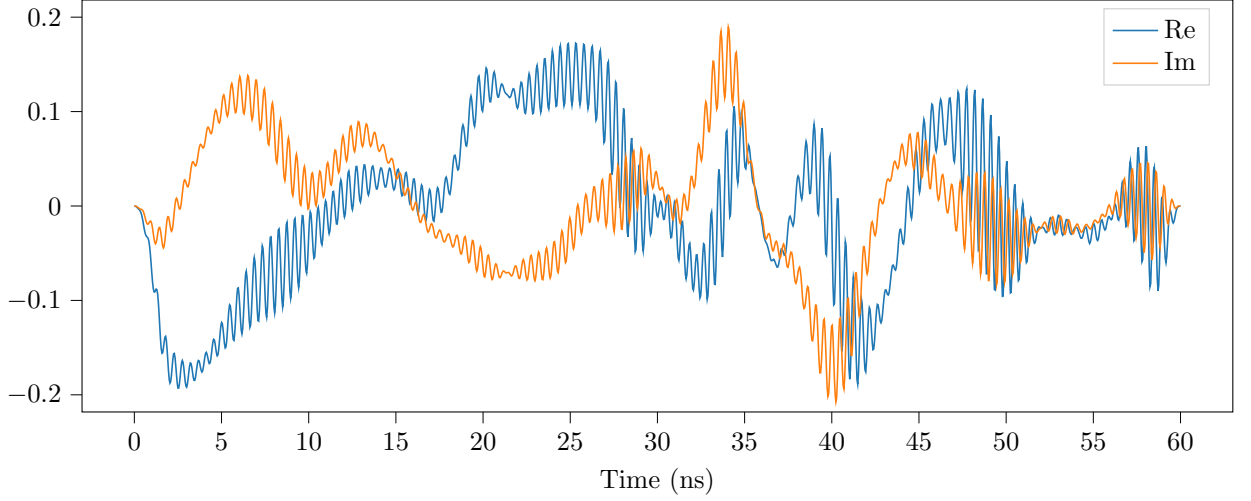
Even though the fidelity goal of $F > 0.999999$ was not reached it could be possible to reach this fidelity goal by decreasing ΔF . Note however that there is no guarantee that such a solution exists.

Looking at the pulse shapes, Figure 5.2, does not give much insight. However, the spectrum shows some interesting phenomena. The qubit control pulse spectrum shows a large peak at the qubit resonance frequency ω_q , as expected, and the same with the resonator and its' resonance frequency ω_r . However there is no clear explanation for the peak at $2\omega_r - \omega_q$ and the peaks of the resonator appearing in the qubit spectrum and vice versa. The width of the resonance peaks for the qubit (resonator) could perhaps be explained by the resonator (qubit) inducing a resonance shift dependent on the state of the qubit (resonator). Consequently, during different times of the pulse the system needs to be driven at a range of frequencies. Further research is needed to explain the characteristics of the solution.

The only discernable “strategy” found, judging by the qubit dynamics in Figure 5.4, is to put the qubit in a superposition which will drive the resonator into the desired state using the coupling. This is in the same



(a) Qubit control pulse shape.



(b) Resonator control pulse shape.

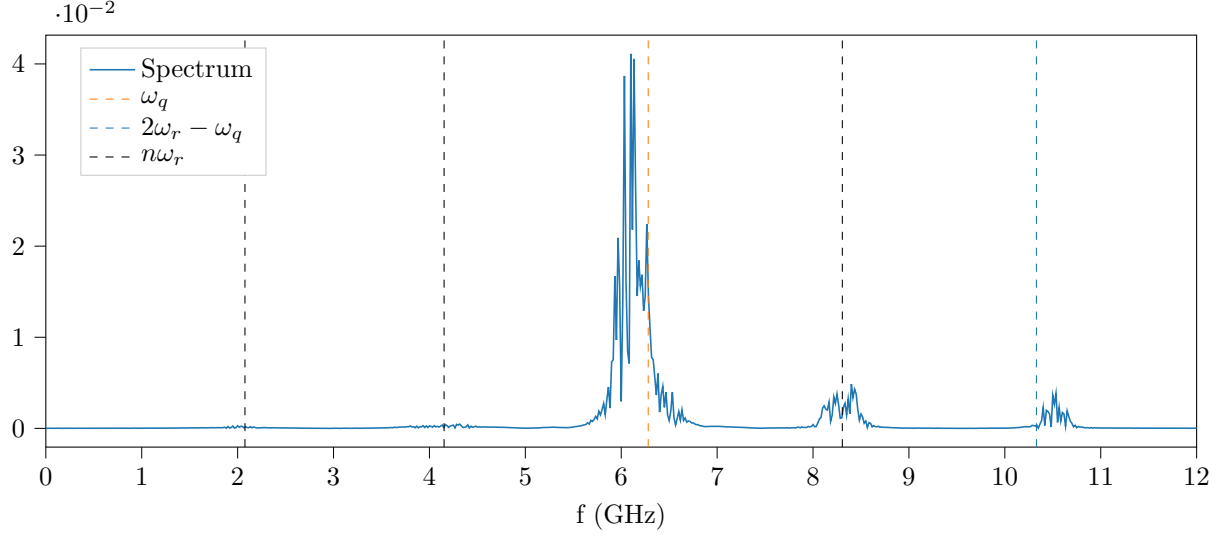
Figure 5.2: Optimized pulse shapes of (a) $\Omega_q(t)$ and (b) $\Omega_r(t)$. The real and imaginary parts of the pulse are shown in blue and orange respectively. The resonator shows rapid oscillations compared to the qubit.

essence as the cat state generation strategy presented in [17]. However, further analysis of the resonator and qubit dynamics and interactions could bring a deeper understanding.

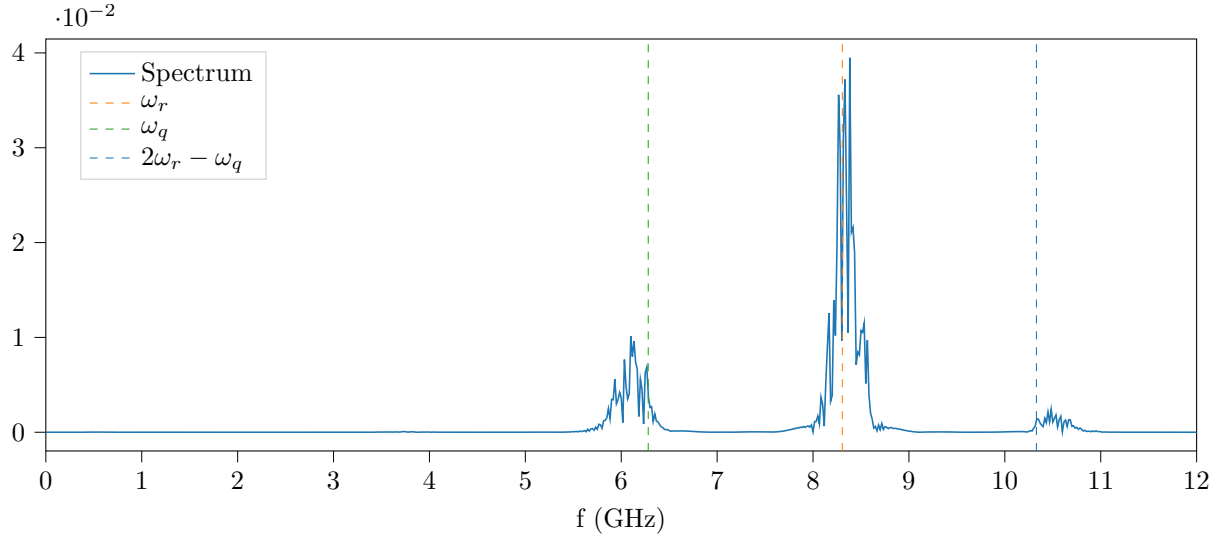
As a perspective of this work, it would be interesting to analyse the limitations of the rotating wave approximation, that we used to derive the Hamiltonian in Equation (5.2). Indeed, the chosen coupling factor is at the edge of the dispersive regime with $g/\Delta \approx 0.11$ and the rotating wave approximation breaks down for anything other than $g/\Delta \ll 1$. This choice was made due to the fact that a larger coupling factor requires less time to realise the transfer. As there was limited time to perform the optimizations, we could use shorter pulse lengths to trade away computational time for less accuracy. We expect the solution to hold, but further accurate solutions might be found within a more general model.

Another consequence of the large coupling factor is that the final state is not robust with respect to small changes in the pulses, as can be seen from the fact that the fidelity goal is reached in the last fraction of a nanosecond. The large coupling will force the qubit and resonator to induce oscillations in each other. These oscillations are probably dependent on the phase of the coupling pulses. As the `krotov` package already provides a way to optimize ensemble objectives with different parameters in each Hamiltonian [18] for robustness, this could be used to optimize for the average of different phase shifts.

Lowering the coupling factor could help mitigate both these issues, however, as stated earlier it is a trade-off. We can perhaps try to speed up the optimization. One way could be to add a mechanism for optimizing pulse



(a) Qubit control pulse spectrum. The black vertical are located at $n\omega_r$ where $n = (0.25, 0.5, 1)$.

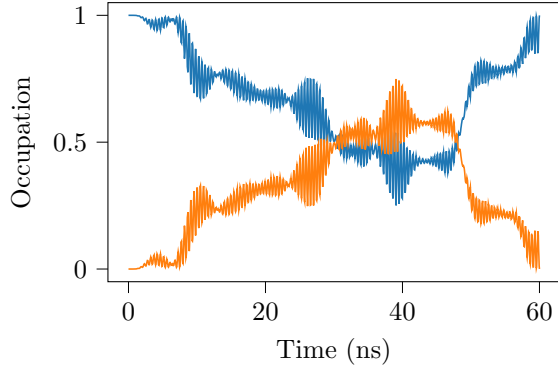


(b) Resonator control pulse spectrum.

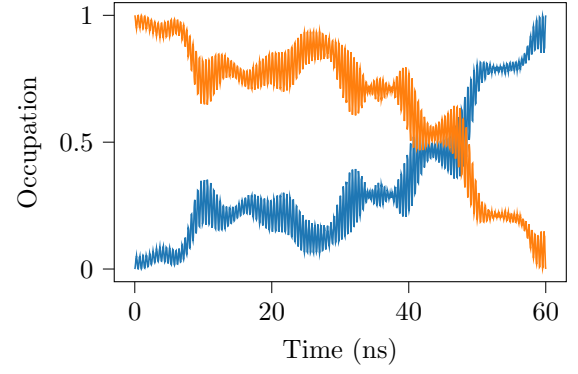
Figure 5.3: Spectrum of optimized pulses (a) $\Omega_q(t)$ and (b) $\Omega_r(t)$ (in the lab frame).

shapes with points sparser than the simulation time grid. Thus one could implement the time-dependent coupling terms separately from the control terms. However if the forward propagation simulation is the most computationally intensive part this would not really help.

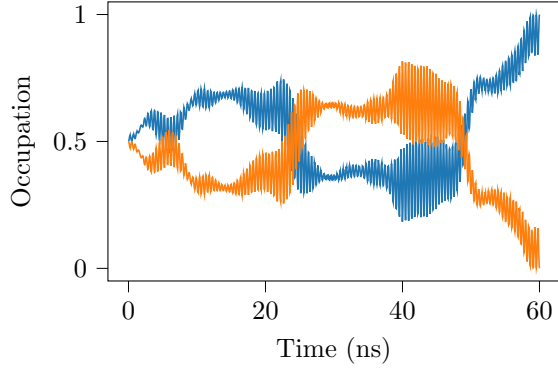
In conclusion, as the qubit transfer simulations showed that **krotov** could optimize simple non-coupled qubits (resonators) with a high fidelity and reasonable physical intuition, this gives support to the validity of the cat code encoding pulses. Even though the underlying theory of the solution is not understood at this moment, Krotov's method proves itself to be able to optimize a state transfer in a qubit-resonator coupled system to a fidelity $F > 0.9990$. Further research need to be done to assess the performance of the pulses in a physical environment, such as including noise which is a significant factor.



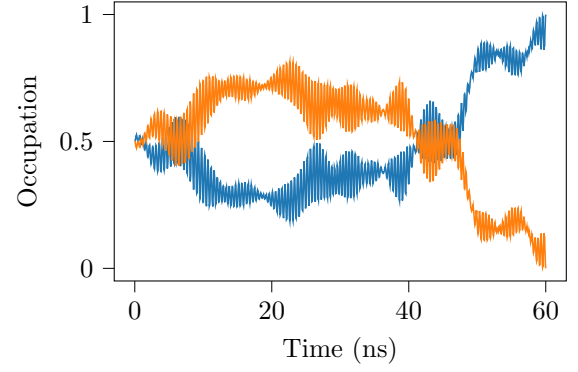
(a) Transfer of $|0\rangle$



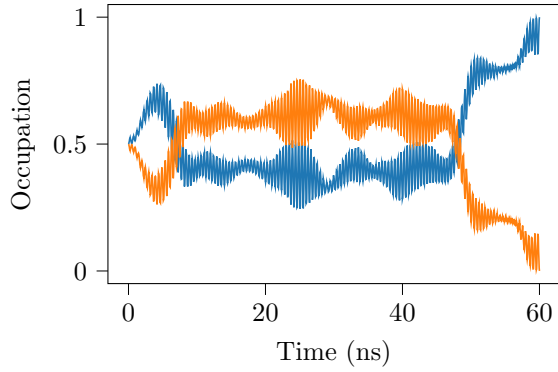
(b) Transfer of $|1\rangle$



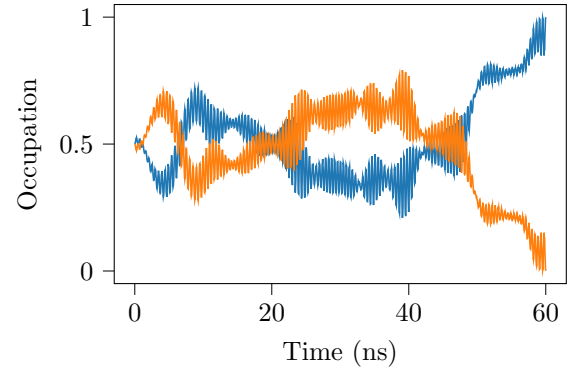
(c) Transfer of $(|0\rangle + |1\rangle)/\sqrt{2}$



(d) Transfer of $(|0\rangle - |1\rangle)/\sqrt{2}$



(e) Transfer of $(|0\rangle + i|1\rangle)/\sqrt{2}$



(f) Transfer of $(|0\rangle - i|1\rangle)/\sqrt{2}$

Figure 5.4: Qubit level occupation over time for the 6 state transfers. $|0\rangle$ and $|1\rangle$ are shown in blue and orange respectively.

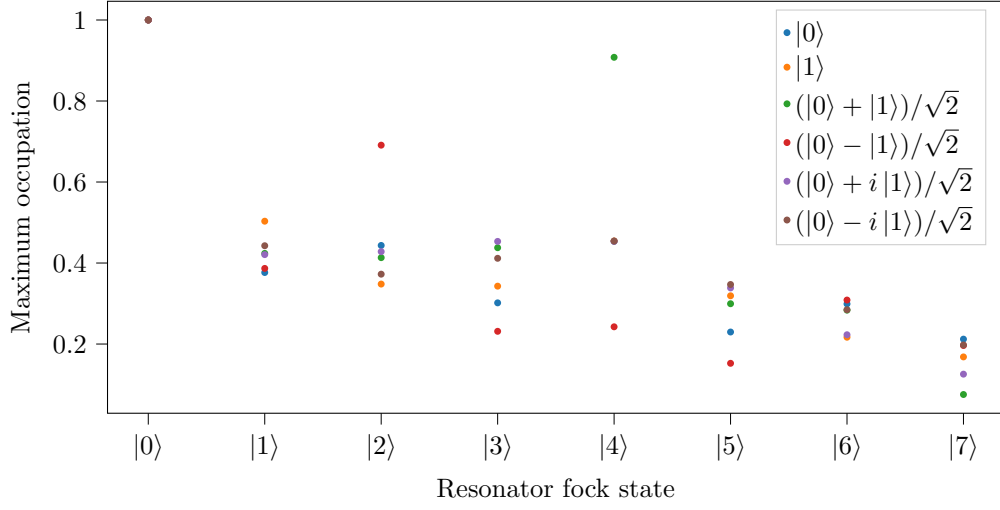


Figure 5.5: Maximum occupation of the Fock basis states for all six state transfers.

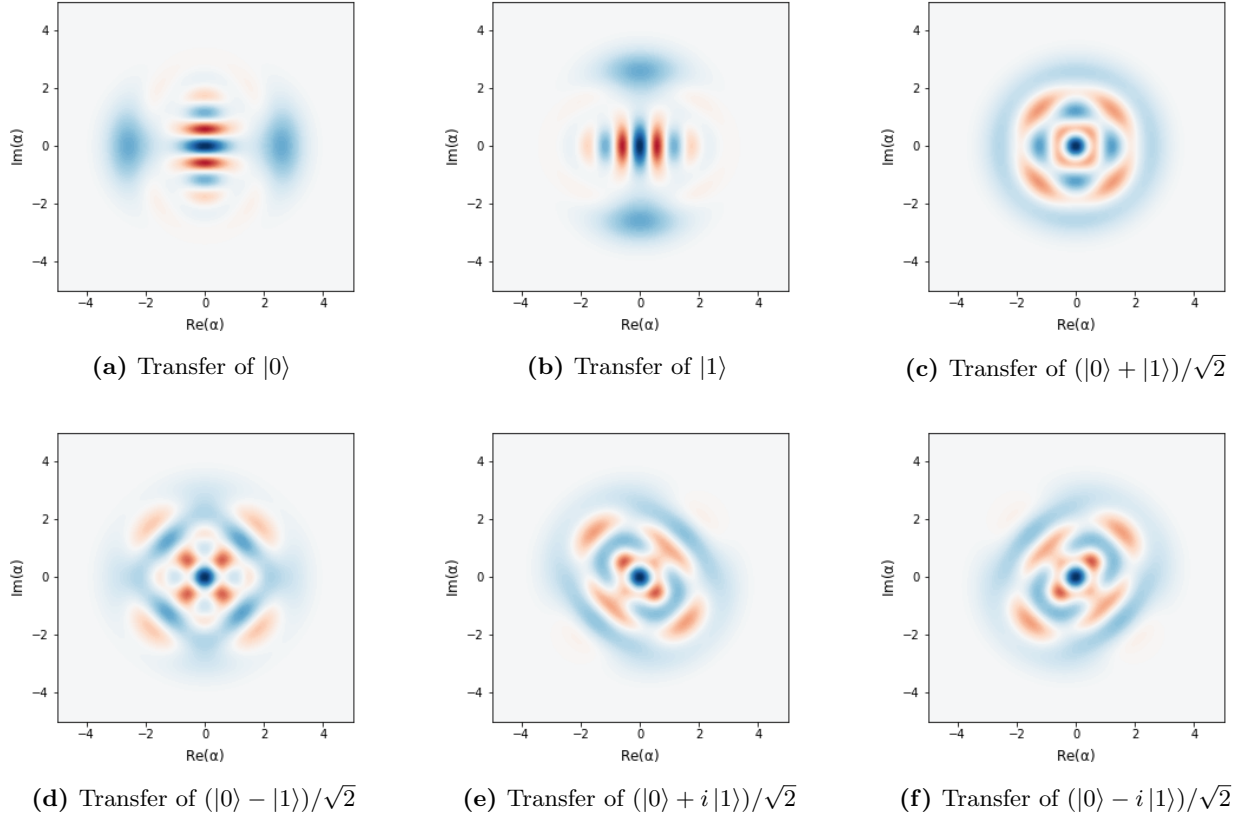


Figure 5.6: Wigner function of the final state (lab frame) of the resonator for all state transfers. The final resonator states are close to the target states shown in Figure A.2.

6 Conclusions

In this chapter some concluding remarks will be presented.

6.1 Conclusive Discussion of the Use of `krotov`

`krotov` provides an easy-to-use interface for setting up optimization problems. This is the strongest argument for using this package as the features are unrivaled compared to other optimization packages. Firstly, QuTiP [16] can optimize with the GRAPE and CRAB algorithms, but there are no provided interfaces for (1) saving optimizations to a file, (2) continuing optimization after they are stopped, (3) optimizing for multiple control fields and objectives, (4) using custom convergence criteria and (5) modifying the pulses after every iteration (for amplitude constraints). These are all critical features which `krotov` has. Secondly, GOAT [19] is a new promising algorithm for quantum optimal control, but has no Python package available yet and the MATLAB implementation has a steep learning curve. If or when the GOAT Python implementation becomes available it would be interesting to compare the feature set and the actual algorithm by testing comparing the performance on the same optimization objective.

The slow convergence of the optimization could pose a problem for larger systems, however there are some techniques for speeding up the optimization which are presented in Section 6.3. If all else fails one could always use more computing power.

6.2 Conclusion of Thesis

In this thesis, we have demonstrated that Krotov's method efficiently realises the $|0\rangle \rightarrow |1\rangle$ evolution for various pulse lengths when supplying guess pulses close to π -pulses. It can also find non-trivial solutions for shorter pulse lengths when an amplitude constraints is present. `krotov` also realises a $|0\rangle \rightarrow |2\rangle$ evolution for various pulse lengths. This proves that `krotov` has potential to be used for non-trivial systems.

Finally and most importantly, we have shown that `krotov` allows to find an optimal pulse solution that allows to control a coupled system composed by a qubit and a resonator, such that the qubit state is dynamically transferred to the resonator by the solution pulse. This procedure is the basis for encoding qubit quantum information into an error correcting code such as a cat code. As the method could realise the transfer for arbitrary qubit states, there is good reason to conclude that `krotov` has the potential to be a valid tool in realising QEC with cat codes. Even though finding the optimal solution is computationally heavy, the pulses only need to be found once in order to be used for encoding. Although many challenges are still unsolved, this proof of concept gives confidence for further research into using `krotov` for finding encoding pulses.

6.3 Future work

As stated in the previous discussions, there are many ways to extend this work. Suggestions for future work are to:

- fix the unrealistic sample rate,
- include dissipation/noise,
- penalize undesired states,
- perform ensemble optimization for different phases of the coupling pulses
- implement a problem-specific system propagator using Cython¹ for speedup and
- find pulses for other bosonic codes.

To encourage the reproduction of these results and further research a link to the source code is given in Appendix A.3.

¹More info: https://krotov.readthedocs.io/en/latest/09_howto.html#how-to-maximize-numerical-efficiency.

References

- [1] J. Preskill, Quantum Computing in the NISQ era and beyond, *Quantum* **2** Aug. 2018, 79, Aug. 2018. DOI: 10.22331/q-2018-08-06-79. [Online]. Available: <http://arxiv.org/abs/1801.00862> (visited on 02/28/2019).
- [2] P. W. Shor, Polynomial-Time Algorithms for Prime Factorization and Discrete Logarithms on a Quantum Computer, *SIAM Journal on Computing* **26**, no. 5 Oct. 1997, 1484–1509, Oct. 1997. DOI: 10.1137/S0097539795293172. [Online]. Available: <http://arxiv.org/abs/quant-ph/9508027> (visited on 01/23/2019).
- [3] R. P. Feynman, Simulating physics with computers, en, *International Journal of Theoretical Physics* **21**, no. 6 Jun. 1982, 467–488, Jun. 1982. DOI: 10.1007/BF02650179. [Online]. Available: <https://doi.org/10.1007/BF02650179> (visited on 02/28/2019).
- [4] A. C. Santos, The IBM Quantum Computer and the IBM Quantum Experience, *Revista Brasileira de Ensino de Física* **39**, no. 1 Sep. 2016, Sep. 2016. DOI: 10.1590/1806-9126-RBEF-2016-0155. [Online]. Available: <http://arxiv.org/abs/1610.06980> (visited on 05/10/2019).
- [5] D. Gottesman, An Introduction to Quantum Error Correction and Fault-Tolerant Quantum Computation, *arXiv:0904.2557 [quant-ph]* Apr. 2009, Apr. 2009. [Online]. Available: <http://arxiv.org/abs/0904.2557> (visited on 05/10/2019).
- [6] Z. Leghtas, G. Kirchmair, B. Vlastakis, R. J. Schoelkopf, M. H. Devoret, and M. Mirrahimi, Hardware-Efficient Autonomous Quantum Memory Protection, *Physical Review Letters* **111**, no. 12 Sep. 2013, 120501, Sep. 2013. DOI: 10.1103/PhysRevLett.111.120501. [Online]. Available: <https://link.aps.org/doi/10.1103/PhysRevLett.111.120501> (visited on 05/10/2019).
- [7] M. Mirrahimi, Z. Leghtas, V. V. Albert, S. Touzard, R. J. Schoelkopf, L. Jiang, and M. H. Devoret, Dynamically protected cat-qubits: A new paradigm for universal quantum computation, *New Journal of Physics* **16**, no. 4 Apr. 2014, 045014, Apr. 2014. DOI: 10.1088/1367-2630/16/4/045014. [Online]. Available: <http://arxiv.org/abs/1312.2017> (visited on 01/29/2019).
- [8] N. Ofek, A. Petrenko, R. Heeres, P. Reinhold, Z. Leghtas, B. Vlastakis, Y. Liu, L. Frunzio, S. M. Girvin, L. Jiang, M. Mirrahimi, M. H. Devoret, and R. J. Schoelkopf, Extending the lifetime of a quantum bit with error correction in superconducting circuits, English, *Nature; London* **536**, no. 7617 Aug. 2016, 441–445, Aug. 2016. DOI: <http://dx.doi.org.proxy.lib.chalmers.se/10.1038/nature18949>. [Online]. Available: <http://search.proquest.com/docview/1815378608/abstract/D91F00AED7CC42E9PQ/1> (visited on 01/23/2019).
- [9] S. M. Girvin, Schrodinger Cat States in Circuit QED, en, *arXiv:1710.03179 [quant-ph]* Oct. 2017, Oct. 2017. [Online]. Available: <http://arxiv.org/abs/1710.03179> (visited on 01/23/2019).
- [10] Y. Wu and X. Yang, Strong-Coupling Theory of Periodically Driven Two-Level Systems, *Physical Review Letters* **98**, no. 1 Jan. 2007, 013601, Jan. 2007. DOI: 10.1103/PhysRevLett.98.013601. [Online]. Available: <https://link.aps.org/doi/10.1103/PhysRevLett.98.013601> (visited on 05/29/2019).
- [11] R. Fisher, “Optimal Control of Multi-Level Quantum Systems”, Dissertation, Technische Universität München, München, 2010.
- [12] D. d’Alessandro, *Introduction to quantum control and dynamics*. Chapman and Hall/CRC, 2007.
- [13] N. Khaneja, T. Reiss, C. Kehlet, T. Schulte-Herbrüggen, and S. J. Glaser, Optimal control of coupled spin dynamics: Design of NMR pulse sequences by gradient ascent algorithms, *Journal of Magnetic Resonance* **172**, no. 2 Feb. 2005, 296–305, Feb. 2005. DOI: 10.1016/j.jmr.2004.11.004. [Online]. Available: <http://www.sciencedirect.com/science/article/pii/S1090780704003696> (visited on 01/30/2019).
- [14] D. M. Reich, M. Ndong, and C. P. Koch, Monotonically convergent optimization in quantum control using Krotov’s method, *The Journal of Chemical Physics* **136**, no. 10 Mar. 2012, 104103, Mar. 2012. DOI: 10.1063/1.3691827. [Online]. Available: <https://aip.scitation.org/doi/10.1063/1.3691827> (visited on 04/29/2019).
- [15] M. H. Goerz, D. Basilewitsch, F. Gago-Encinas, M. G. Krauss, K. P. Horn, D. M. Reich, and C. P. Koch, Krotov: A Python implementation of Krotov’s method for quantum optimal control, *arXiv:1902.11284 [quant-ph]* Feb. 2019, Feb. 2019. [Online]. Available: <http://arxiv.org/abs/1902.11284> (visited on 03/13/2019).
- [16] J. R. Johansson, P. D. Nation, and F. Nori, QuTiP 2: A Python framework for the dynamics of open quantum systems, *Computer Physics Communications* **184**, no. 4 Apr. 2013, 1234–1240, Apr. 2013. DOI:

- 10.1016/j.cpc.2012.11.019. [Online]. Available: <http://arxiv.org/abs/1211.6518> (visited on 05/28/2019).
- [17] S. Haroche and J.-M. Raimond, *Exploring the quantum: atoms, cavities, and photons*. Oxford university press, 2006.
 - [18] M. H. Goerz, E. J. Halperin, J. M. Aytac, C. P. Koch, and K. B. Whaley, Robustness of high-fidelity Rydberg gates with single-site addressability, *Physical Review A* **90**, no. 3 Sep. 2014, 032329, Sep. 2014. DOI: 10.1103/PhysRevA.90.032329. [Online]. Available: <https://link.aps.org/doi/10.1103/PhysRevA.90.032329> (visited on 06/02/2019).
 - [19] S. Machnes, E. Assémat, D. J. Tannor, and F. K. Wilhelm, Gradient optimization of analytic controls: The route to high accuracy quantum optimal control, *Physical Review Letters* **120**, no. 15 Jul. 2015, Jul. 2015. DOI: 10.1103/PhysRevLett.120.150401. [Online]. Available: <http://arxiv.org/abs/1507.04261> (visited on 03/14/2019).
 - [20] Glosser.ca, *English: Bloch sphere; a geometrical representation of a two-level quantum system. Rendered with Asymptote*. Dec. 2012. [Online]. Available: https://commons.wikimedia.org/wiki/File:Bloch_Sphere.svg (visited on 05/22/2019).

A Appendix

A.1 Bloch Sphere Visualization

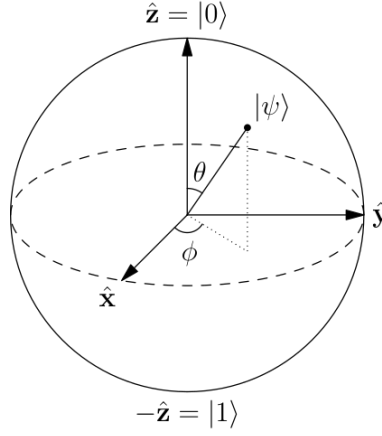


Figure A.1: Representation of an arbitrary pure quantum state on the Bloch sphere.
Source: [20] (CC BY-SA 3.0).

The pure state of a qubit can be visualized on the surface of a unit sphere with the following parametrization

$$|\psi\rangle = \cos\left(\frac{\theta}{2}\right) |0\rangle + e^{i\phi} \sin\left(\frac{\theta}{2}\right) |1\rangle \quad (\text{A.1})$$

where θ and ϕ are the angles shown in Figure A.1. The ground state $|0\rangle$ is located on the “north pole” and the excited state $|1\rangle$ on the “south pole”.

Further, a handy trick to visualize the qubit when it has more than two levels is to “project” the state to the $\{|0\rangle, |1\rangle\}$ basis with $|0\rangle\langle 0| + |1\rangle\langle 1|$ and then plot it on the Bloch sphere. This means that the subspace which is not spanned by the first two levels will be represented by the inside of the sphere. For example, the state $|2\rangle$ will lie right in the center of the sphere while $(|1\rangle + |2\rangle)/\sqrt{2}$ will lie halfway between the center and the south pole.

A.2 Cat Code Supplementary Figures

A.2.1 Wigner Function of Resonator Target States

The six target states in the cat code basis are shown in Figure A.2 with $\alpha = 2$ and a Hilbert space truncated at a size of $N_r = 8$. Looking at the Wigner function of $|0\rangle$ in (the logical cat code basis), we can see two lobes with an interference fringe in between them. For large enough N_r the lobes will appear circular. Compared to the basis states, the superposition states exhibit even more complex shapes.

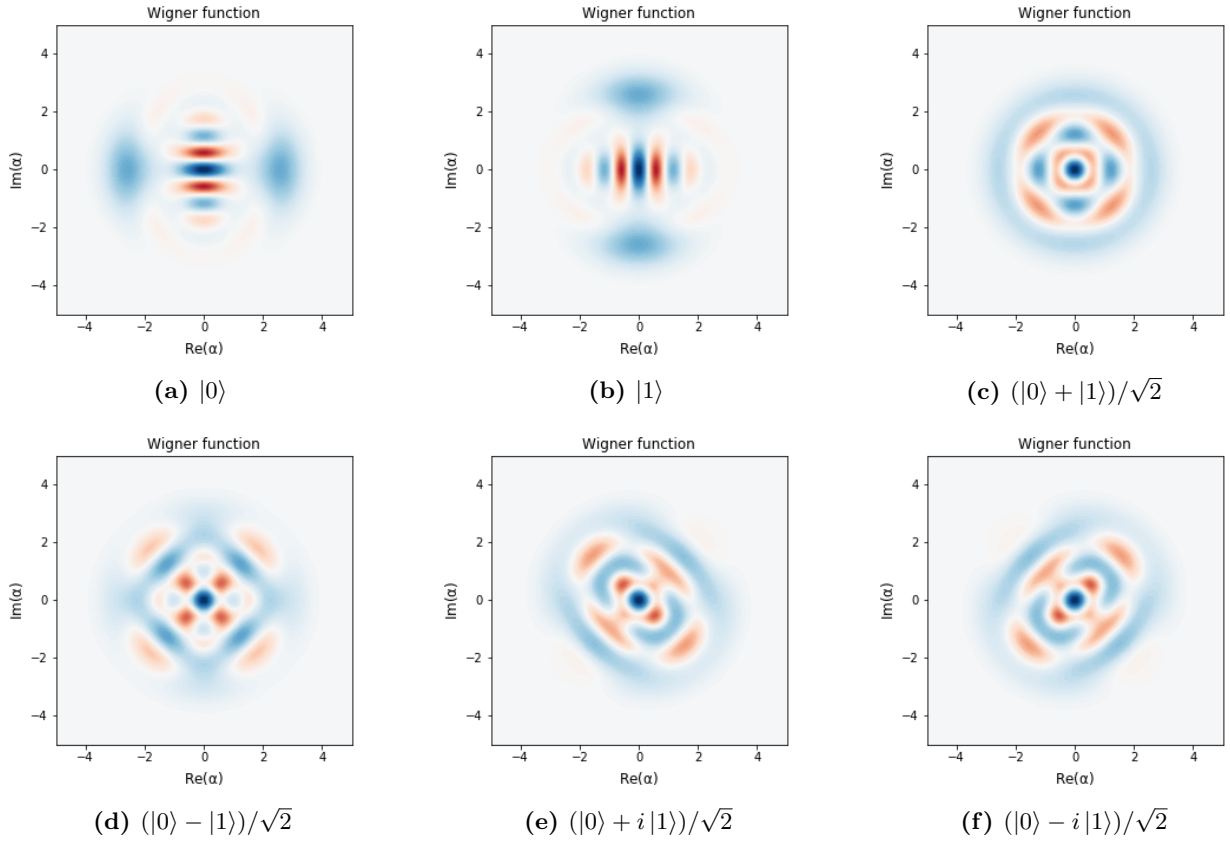
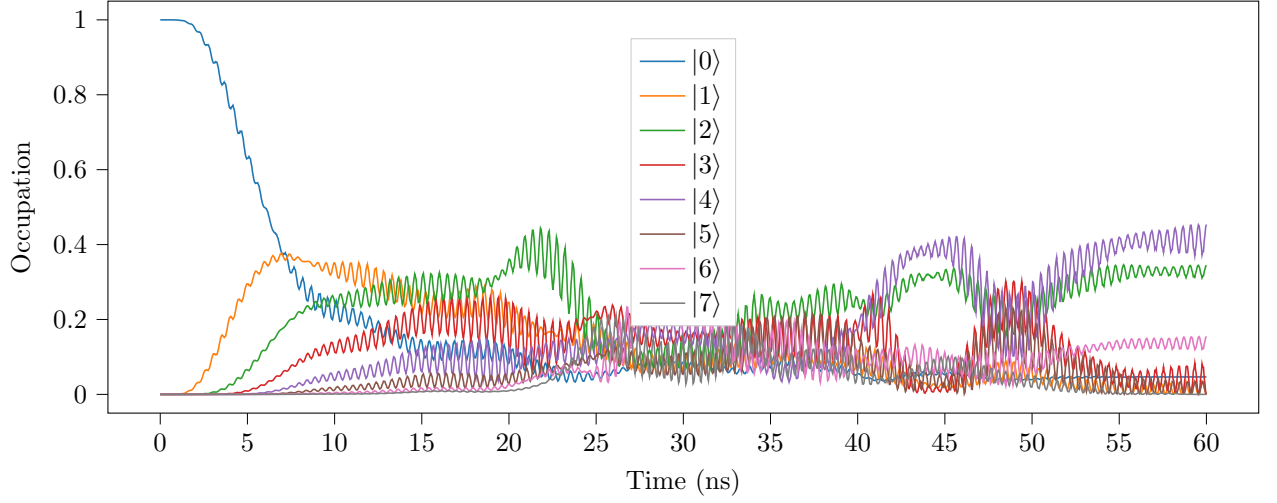


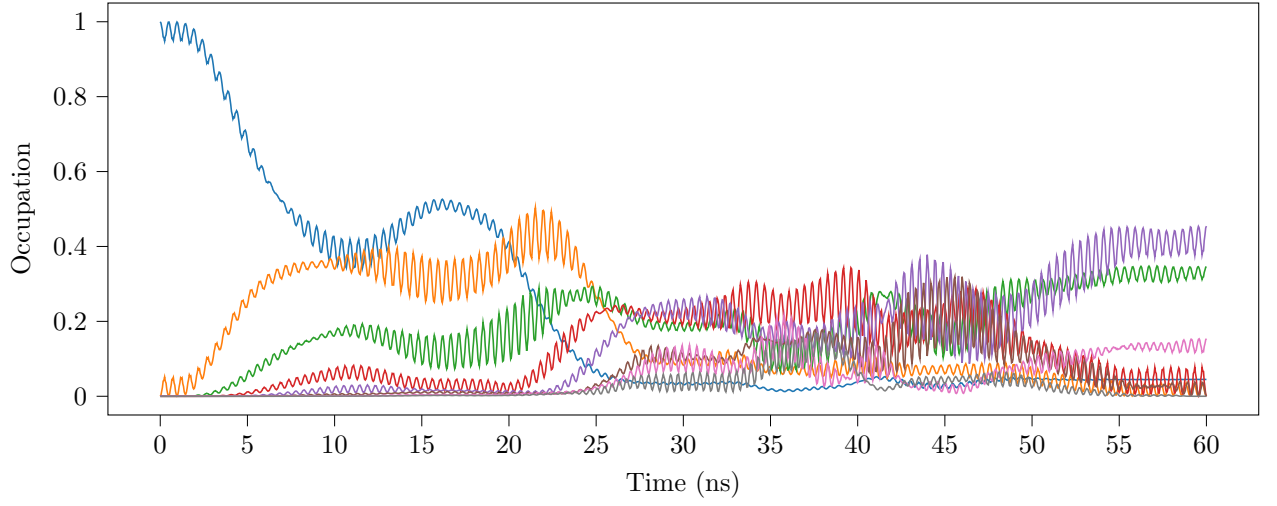
Figure A.2: Wigner function of the six target states in the cat code basis with $\alpha = 2$ and $N_r = 8$.

A.2.2 Occupation Dynamics of Resonator During State Transfer

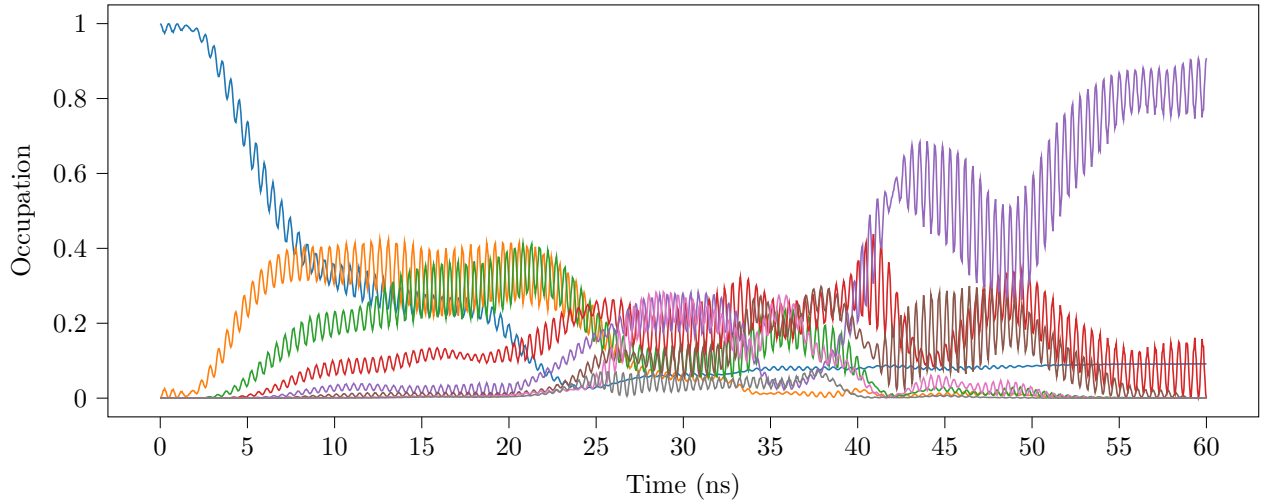
The occupation dynamics for the resonator during the state transfer are plotted in Figure A.3.



(a) Transfer of $|0\rangle$

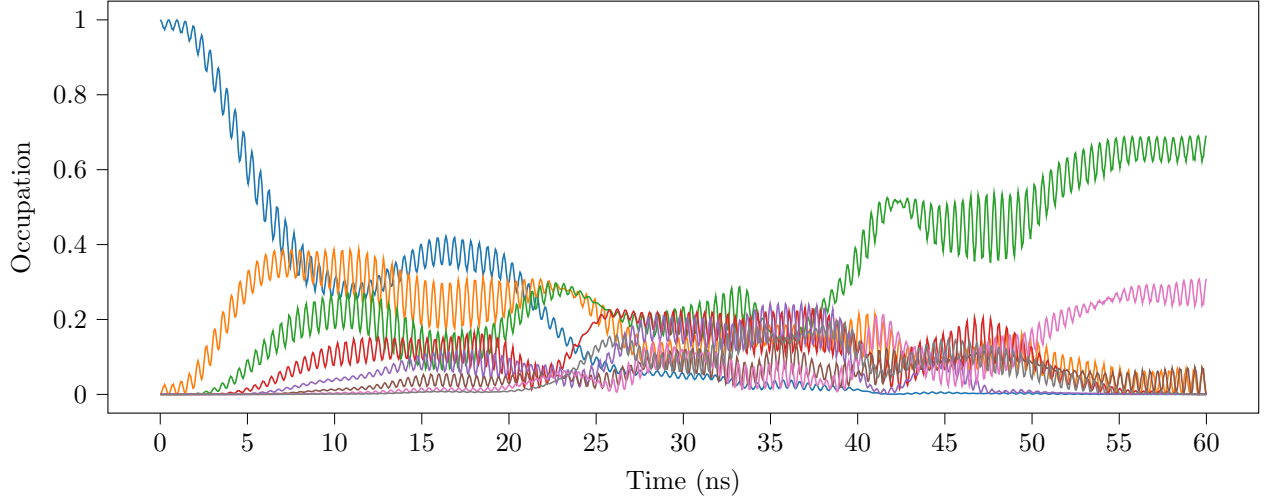


(b) Transfer of $|1\rangle$

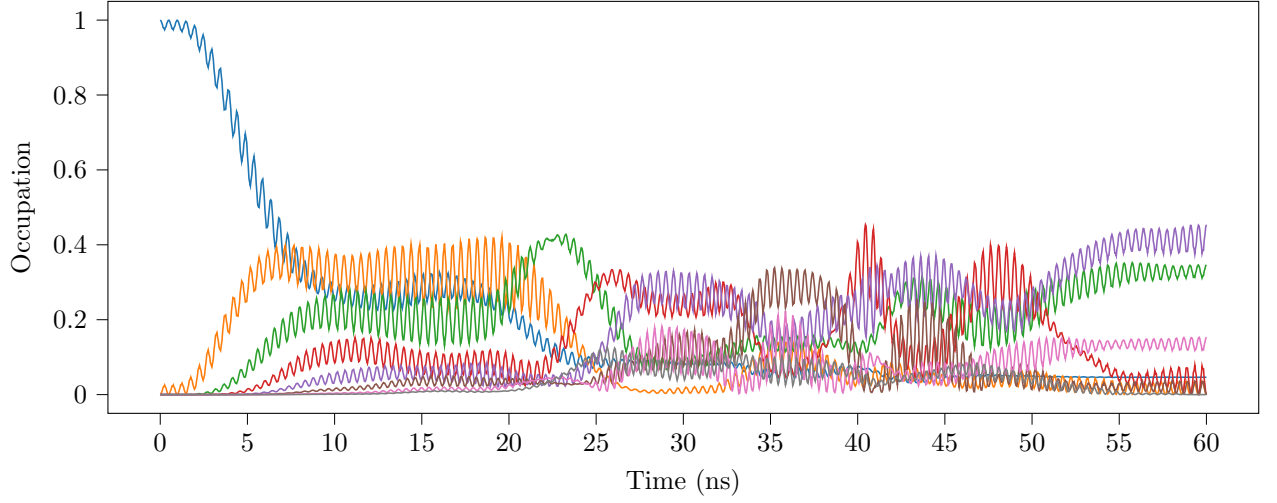


(c) Transfer of $(|0\rangle + |1\rangle)/\sqrt{2}$

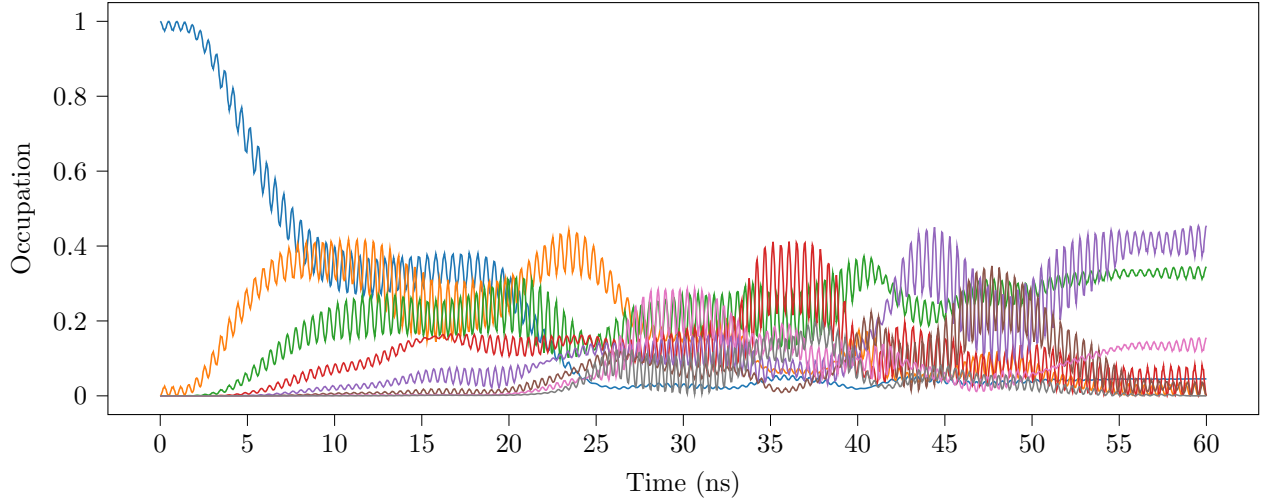
Figure A.3: Resonator level occupation over time for the 6 state transfers.



(d) Transfer of $(|0\rangle - |1\rangle)/\sqrt{2}$



(e) Transfer of $(|0\rangle + i|1\rangle)/\sqrt{2}$



(f) Transfer of $(|0\rangle - i|1\rangle)/\sqrt{2}$

Figure A.3: Resonator level occupation over time for the 6 state transfers.

A.3 Jupyter Notebooks and Optimization Data

To ease the reproducibility of the simulations the Jupyter notebooks used in this thesis and majority of resulting data are available at <https://github.com/JohanWinther/cat-state-encoding>. Even though the code isn't provided in a structured fashion it will still be provided publicly so as to encourage code and data sharing.